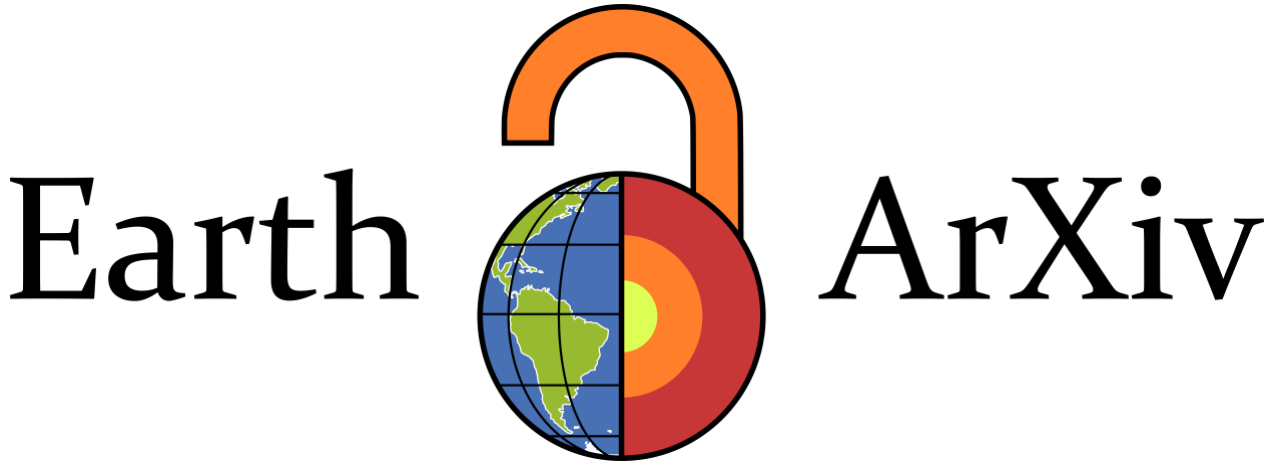



This is a non-peer-reviewed preprint submitted to EarthArXiv.

---

This manuscript has been submitted for publication in *Journal of Glaciology*. Please note the manuscript has yet to be formally accepted for publication. Subsequent versions of this manuscript may have slightly different content. If accepted, the final version of this manuscript will be available via the 'Peer-reviewed Publication DOI' link on the right-hand side of this webpage. Please feel free to contact any of the authors; we welcome feedback.

---

# *Drivers of The Daggers*: Backstress-triggered fracture propagation on the Thwaites Eastern Ice Shelf, West Antarctica

Meghan A. SHARP[1], Erin C. PETTIT[1]*, Karen E. ALLEY[2], Martin TRUFFER[3], Atsuhiro MUTO[4], Adrian LUCKMAN[5], Christian T. WILD[1,6], Genevieve SAURET[1]

[1]*College of Earth, Ocean, and Atmospheric Science, Oregon State University, Corvallis, OR, USA;*

[2]*Centre for Earth Observation Science, Department of Environment and Geography, University of Manitoba, Winnipeg, MB, Canada*

[3]*Geophysical Institute and Dept. Physics, University of Alaska Fairbanks, Fairbanks, Alaska, AK, USA;*

[4]*Department of Earth and Environmental Science, Temple University, Philadelphia, PA, USA;*

[5]*Department of Geography, Faculty of Science and Engineering, Swansea University, UK;*

[6]*Department of Atmospheric and Cryospheric Sciences (ACINN), University of Innsbruck, Innsbruck, Austria*

*Correspondence: Meghan A. Sharp <sharpmeg@oregonstate.edu>*

**ABSTRACT.**

**The destabilization of ice shelves around Antarctica is not just a sea-level-rise priority, but an opportunity to observe and understand the mechanisms of ice-shelf failure. Recent studies show that ice shelves fail against their pinning points or ridges once sufficiently weakened by thinning and damage—a "backstress-triggered" failure mechanism that is not represented in ice-shelf collapse criteria employed by ice-sheet models. We suggest that fractures extending upstream from a pinning point/ridge are a signature of backstress-triggered failure. In this study, we identify controls on the spatiotemporal evolution of five such fractures on the Thwaites Eastern Ice Shelf. Vertical propagation may have been limited by a heterogeneous layer above the fracture tip, which penetrates ~70–80% of the ice column, as revealed by ice-**

*Present address: College of Earth, Ocean, and Atmospheric Sciences, Oregon State University, Corvallis, Oregon, USA.

**penetrating radar. Horizontal propagation is correlated with relatively small, ∼10°, fluctuations in the direction of ice flow in response to a weakening shear zone against the pinning ridge, possibly modulated by a change in ice thickness at the fracture tips. In hindsight, we suggest this style of fracture has occurred during other ice-shelf breakups around Antarctica. As an observable indicator that backstress-triggered ice-shelf failure is underway, these fractures may be a promising avenue towards a new collapse criterion.**

## INTRODUCTION

Ice shelves, the floating extensions of glaciers, typically rely on resistive stresses from submarine seamounts, islands, or fjord walls for structural support. These anchors, or pinning points, are the foundations of an ice shelf's buttressing ability, that is, it's ability to slow ice flow across the grounding line and modulate global sea level. However, recent observations have highlighted a shift in the role of pinning points during the later stages of ice-shelf breakup—from stabilizing features to sources of destabilization (e.g. Benn and others, 2022; Banerjee and others, 2025b; Walker and others, 2024; Wild and others, 2024; Alley and others, 2021). This transition is poorly understood, but is fundamental for achieving accurate predictions of ice-shelf stability and the response of the ice sheets to climatic and oceanic change.

Until recently, hydrofracture was assumed to be the dominant mechanism of ice-shelf breakup. This paradigm emerged due to an observational link between regional climate warming, longer melt seasons, and the presence of surface melt ponds during many of the breakups that occurred early in the satellite record, particularly the Wordie, Larsen A, Larsen B, and Wilkins ice shelves that fringe the Antarctic Peninsula and collapsed in the 1980s to early 2000s (e.g. Vaughan and Doake, 1996; Scambos and others, 2000; van den Broeke, 2005; Skvarca, 1993; Rott and others, 1998; Scambos and others, 2003; Shepherd and others, 2003; Scambos and others, 2009). Observations of ice-shelf breakup in the absence of surface melt in the past decade, however, have shifted this paradigm and led to two alternative mechanisms of break-up: *unpinning*, when an ice shelf thins and loses contact with its pinning point, as in the case of the Thwaites Glacier Tongue (Tinto and Bell, 2011; Miles and others, 2020), and *backstress-triggered failure*, when an ice shelf is sufficiently weakened such that it can no longer withstand the backstess from its pinning point and begins to fracture, as observed on the Thwaites Eastern (TEIS) (Benn and others, 2022; Banerjee and

others, 2025b; Wild and others, 2024; Alley and others, 2021) and Conger-Glenzer ice shelves (Walker and others, 2024).

Despite the range of proposed ice-shelf breakup mechanisms, ice-sheet models currently lack a rigorous treatment of ice-shelf removal due to limited physical understanding of the processes involved (Arthur and others, 2026). Typically, the removal of ice shelves is implemented with a collapse criterion that requires a threshold rate of surface melting for 10 years or more, based on observations of hydrofracture (Seroussi and others, 2020). Models that do not require surface melting remove ice shelves with either a prescribed calving-front position or retreat rate, or they remove floating ice below a minimum thickness (Seroussi and others, 2020; Barnes and others, 2026). Burgard and others (2025) recognize the need for a more complete treatment of ice-shelf processes and include both a surface and basal mass balance, as well as a calving flux in their model of ice shelf viability across Antarctica. Without any representation of the aforementioned breakup mechanisms, the viability of ice shelves such as TEIS are severely overestimated when compared with observations, predicting stability for centuries (Burgard and others, 2025) rather than years to decades (Alley and others, 2021; Wild and others, 2022). A process-scale understanding of the observed ice-shelf breakup mechanisms is pivotal for developing new collapse criteria.

Accurate predictions of ice-shelf loss are of particular importance at Thwaites Glacier, one of the largest drainage basins of the West Antarctic Ice Sheet, which has the potential to contribute metres to global sea level (Bamber and others, 2009). Grounded below sea level on a retrograde bed slope (e.g. Morlighem and others, 2020), Thwaites Glacier is vulnerable to irreversible retreat (Yu and others, 2018; Seroussi and others, 2017; Joughin and others, 2014) and relies in part on the resistive forces provided by its ice shelves for stability (e.g. dos Santos and others, 2021). However, an increased presence of modified Circumpolar Deep Water (mCDW) on the continental shelf in the Amundsen Sea has driven substantial basal melting (e.g. Jacobs and others, 2011; Dutrieux and others, 2014; Holland and others, 2019) and led to thinning and fracture of the floating extensions of Thwaites Glacier (Miles and others, 2020; Chartrand and others, 2024; Alley and others, 2021; Wild and others, 2022; Benn and others, 2022; Wild and others, 2024; Banerjee and others, 2025b). Acceleration of grounded ice in response to this loss of buttressing has been observed (Wild and others, in prep) and some studies suggest that the irreversible retreat of the West Antarctic Ice Sheet is already underway (Joughin and others, 2014; Rignot and others, 2014). Thus, further understanding the Thwaites Glacier system remains a priority, and the decade-old sea-level-rise question endures— "how much, how fast?" (Scambos and others, 2017).

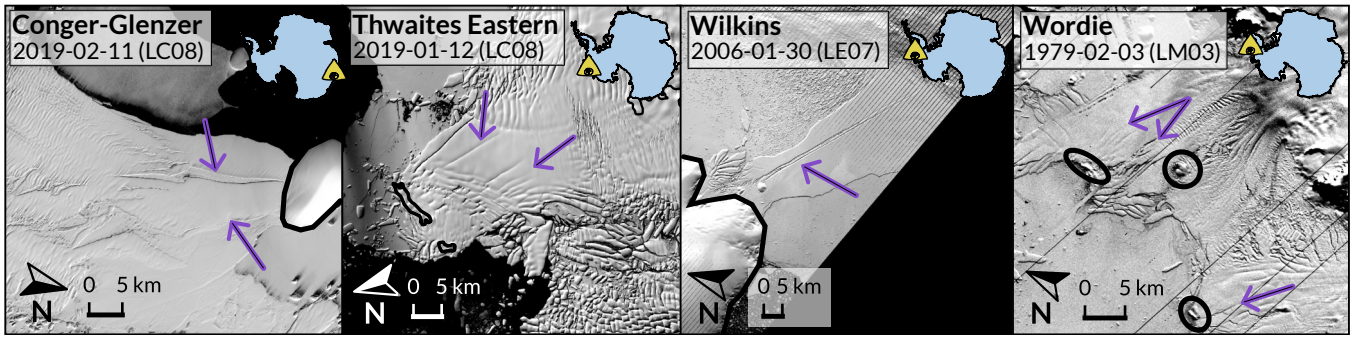



**Fig. 1. Backstress-failure fractures during ice-shelf breakups.** Landsat images with fractures denoted by purple arrows and pinning point locations shown by black polygons. Images are in Antarctic Polar Stereographic, with north arrows pointing to True North and ice-shelf locations shown by the Scott Tent (yellow triangle) on the inset map of Antarctica.

Thwaites Glacier is not just a sea-level-rise priority, but also an opportunity. The ongoing destabilization of its last remaining ice shelf, TEIS, provides a unique opportunity to observe backstress-triggered ice-shelf failure with more detailed satellite and field observations than previously available. Recent work has focused on the development and evolution of fractures in a shear zone immediately upstream of its pinning point (a submarine ridge) (Benn and others, 2022; Banerjee and others, 2025b), which we summarize in the next section. In this study, we investigate an additional set of fractures that extend orthogonally from the submarine ridge, upstream into the otherwise relatively intact body of the ice shelf (Figures 1 & 2; Alley and others, 2021; Benn and others, 2022; Wild and others, 2024; Banerjee and others, 2025b). We refer to these fractures as *the Daggers* as they cut like daggers through the "heart" of TEIS. A similar style of fractures are observed in the decade(s) leading up to the breakup of the Conger-Glenzer, Wilkins, and Wordie ice shelves (Figure 1) and are often the loci of the final large calving events (Walker and others, 2024; Braun and Humbert, 2009; Braun and others, 2009; Dømgaard and others, 2025).

A key question facing potential models and parameterizations of backstress-triggered ice-shelf breakup is, what controls when an ice shelf has become sufficiently weakened such that it can no longer withstand backstress from its pinning point(s)? This threshold marks a transition to pinning-point-driven destabilization. An easily observable indicator may be the presence of the aforementioned fractures that extend upstream from pinning points, hereafter termed *backstress-failure fractures*. Although there have been individual studies of their formation (e.g. Wild and others, 2024; Walker and others, 2024; Braun and Humbert, 2009), the commonality of backstress-failure fractures across ice shelves has only recently been identified (Alley and others, in review), leaving the processes governing their evolution largely unknown.

In this study, we identify controls on the propagation of the Daggers on TEIS, as they formed and evolved with a wealth of satellite and field data (Figure 2).

We structure this paper as follows. After presenting the details of the data and methods, we 1) describe the fracture geometry from ice-penetrating radar, and 2) contextualize phases of fracture propagation within the changing stress regime of TEIS over the past decade (2016-2026) using satellite-derived velocities, strain rates, and digital elevation models (DEMs). We then discuss factors that may favour or inhibit both vertical and horizontal fracture propagation, and use a simple numerical model to aid our discussion. We conclude by briefly placing this discussion in the context of other ice shelves.

## STUDY SITE: The ongoing destabilization of Thwaites Eastern Ice Shelf

TEIS is supported by a pinning point at its downstream margin, a linear submarine ridge that has two prominent sections in contact with the ice shelf, one 9 km long and the other 2.5 km, with a 4 km space in between, based on grounding line estimates representative of 2019/20 (Wild and others, 2022) (polygons in Figure 4). Thus, we hereafter refer to it as the *pinning ridge*. The ice shelf is approximately 50-km long from the grounding line to the pinning ridge, 65-km wide near the grounding zone, and 20-km wide across the main shelf (Figure 2). TEIS has two calving fronts, one at each of its eastern and western margins. The eastern margin is unconfined and a prominent shear zone exists at the western margin between TEIS and the Thwaites Glacier Tongue (TGT-TEIS shear margin, Figure 2 b). The TGT-TEIS shear margin has historically had a significant influence on the dynamics of TEIS (Alley and others, 2021) and was comprised of ice mélange until a sea ice breakout in 2023 left most of the downstream portion of the margin as open seawater, apart from intermittent sea ice (Figure 2d).

Fracturing in the absence of surface water plays a pivotal role in the ongoing destabilization of TEIS (Alley and others, 2021; Wild and others, 2022; Benn and others, 2022; Wild and others, 2024; Banerjee and others, 2025b), where meltwater is typically retained in the porous firn layer rather than accumulating in surface ponds (Dunmire and others, 2024). Hence, there is no evidence of hydrofracture on TEIS at present. Over the past two decades, full-thickness rifts have opened and widened near the present-day grounding zone (Wild and others, 2024), a crevasse swarm opened near the mid-2000s grounding zone and has advected to the main ice shelf (Alley and others, 2021), large shear fractures have developed across the pinning-point margin (Figure 2; Benn and others, 2022; Banerjee and others, 2025b), and a set of five parallel fractures (the Daggers) have propagated from the pinning ridge through the central part of the ice

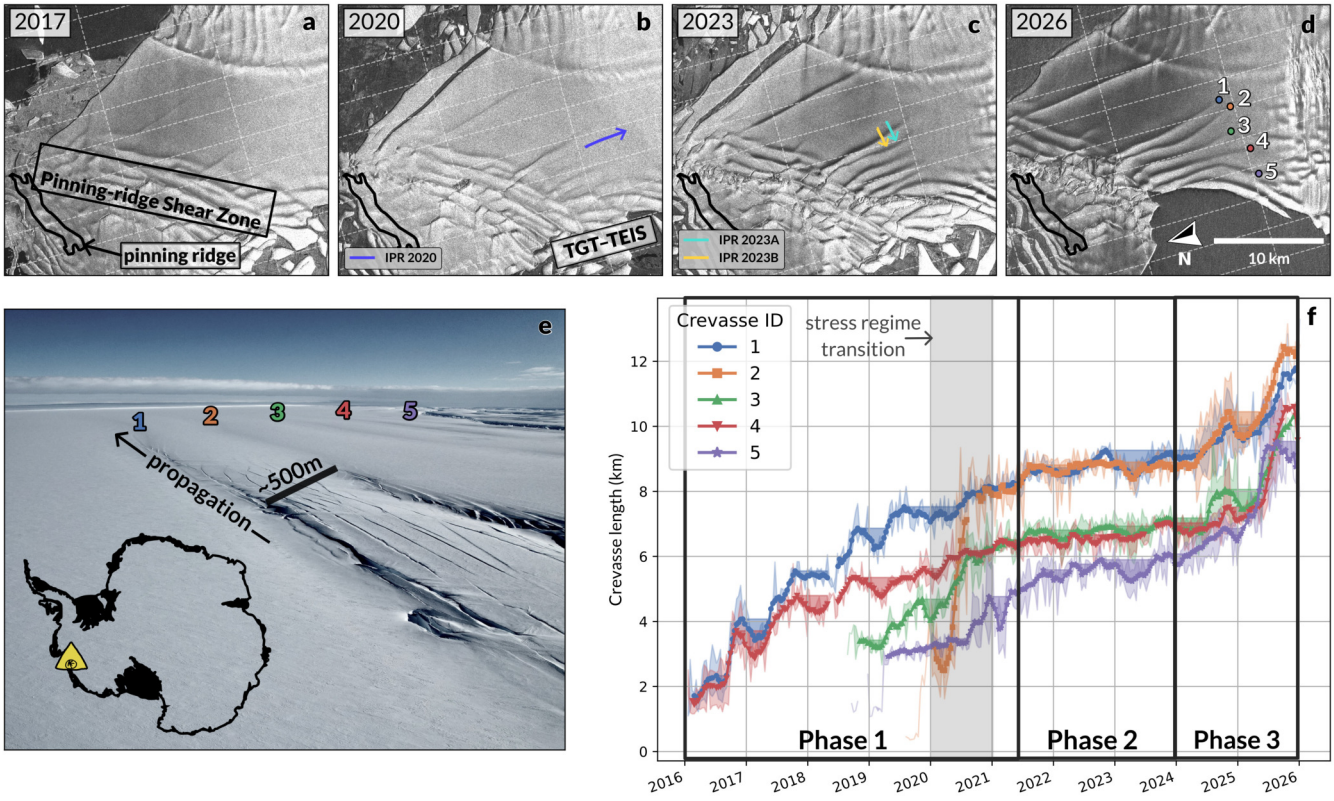



**Fig. 2. Evolution of backstress-failure fractures (the Daggers) on TEIS between 2016 and 2026.** (a-d) Sentinel-1 Synthetic Aperture Radar (SAR) images of the ice shelf acquired in January of each labelled year. Black lines denote the 2019/20 grounding line, i.e. pinning ridge (Wild and others, 2022). Coloured lines denote Ice-Penetrating Radar tracks collected in January of 2020 (b) and 2023 (c). Numbers 1–5 in (d) correspond to crevasse IDs referred to in this study. Lines of latitude and longitude are shown in intervals of 0.1° with white dashed lines. (e) Drone image of the surface depressions (shadows) overtop of the Daggers. Image is looking towards the tips in January 2023. The location of TEIS is denoted by the Scott tent (yellow triangle) on the inset map of Antarctica. (f) Time series of crevasse length for the five crevasses labelled in panel d, derived from two independent manual digitizations of Sentinel-1 SAR images. Symbols and thick lines denote the mean of the two digitizations, smoothed with a window length of 60 days. The light shaded envelope denotes the full range between digitizers (minimum–maximum), representing inter-digitizer variability. The dark shaded envelope denotes the cumulative maximum of the smoothed mean curve, as apparent "shortening" of crevasses is due to variability between SAR images, not physical shortening of the crevasses.

shelf (Figure 2, Benn and others, 2022; Wild and others, 2024).

One of the most pronounced structural changes on TEIS over the past decade was the development of a highly fractured shear margin immediately upstream of the pinning ridge as it transitioned from a

stabilizing feature to a destabilizing one. This shear zone, hereafter referred to as the *Pinning-ridge Shear Zone* (Figure 2a), effectively disconnected the main ice shelf from the pinning ridge by 2022—a process that began decades prior (Benn and others, 2022; Banerjee and others, 2025b). Observations (Alley and others, 2021; Banerjee and others, 2025b) and numerical experiments (Benn and others, 2022) show that the Pinning-ridge Shear Zone developed in response to an acceleration of the ice shelf between 2002 and 2006, which seeded a positive feedback between damage and strain (Åström and Benn, 2019; Lhermitte and others, 2020). The final stage of the shear-zone development led to an extensional stress regime upstream of the pinning ridge between 2017 and 2022 (Banerjee and others, 2025b), yielding the Daggers through the central part of the shelf (Figure 2).

The Daggers are oriented approximately perpendicular to the pinning ridge, ∼130° to the Pinning-ridge Shear Zone, and are spaced 900-1400 m apart (2.5–3.5 times the local ice thickness). The fractures propagated episodically between 2016 and mid-2021, until the rate of propagation slowed and they appeared to stagnate between mid-2021 and 2024 (Wild and others, 2024). We show that the fractures re-activated again between January–June 2024 (Figure 2 f). As of January 2026, most of these basal fractures have not yet penetrated to the ice-shelf surface and are only visible in satellite imagery due to the depressions formed by ongoing hydrostatic adjustment.

Overall, the underlying drivers of these propagation patterns remain poorly understood, despite their potential to seed rifts and icebergs in the eventual break-up of TEIS and their broader significance in understanding backstress-triggered ice-shelf breakup. Here, we do not attempt to explain each individual propagation event (previously documented by Wild and others, 2024). Rather, we relate the multi-year temporal patterns, or *phases*, of fracture propagation to ice shelf-scale changes in the stress regime of TEIS.

# METHODS

## Satellite-image analysis

With the goal of tracking patterns of crevasse growth through time and space, we compiled and manually digitized the Daggers in Sentinel-1 Synthetic Aperture Radar (SAR) images between January 2016 and January 2026, with continued coverage through cloud cover and polar night/austral winter. The image set contains a total of 299 images that were acquired along the descending track with a 12–day repeat interval and resampled to a pixel size of 10 m.

Similar to Wild and others (2024), we manually digitized the surface depressions of the Daggers in each

SAR image. However, we traced the entire shape of the crevasse as a line feature, whereas Wild and others (2024) calculated the Euclidean distance between manually chosen points at the beginning and end of each crevasse. We also extend the time series to the end of 2025. For ease of reference, we denote the fractures as Crevasses 1–5 in spatial order from east to west across the ice shelf (Figure 2).

Manually discerning the endpoints of surface depressions in the SAR imagery is inherently subjective. To estimate human-related uncertainty, the image set was digitized twice, each by a different analyst. Each dataset was digitized in a different temporal direction: one analyst digitized forward in time from 2016 to 2026 and the other backwards from 2026 to 2016. We report the crevasse length as the mean of the two independently digitized datasets smoothed by a 60-day running mean in Figure 2 f, with error envelopes corresponding to the maximum and minimum of the two independent raw measurements. We note that the apparent shortening of crevasses in Figure 2 f represents error due to changes in surface reflectance in the Sentinel-1 scenes, not physical shortening of the crevasses. Thus, we overlay an additional error envelope as the cumulative maximum of the smoothed mean curve.

The digitized surface depression likely lags the actual fracture propagation, as the surface depression is a viscoelastic response of the ice to the initial fracture and subsequent widening due to melt and potentially necking (Bassis and Ma, 2015). However, assuming that the lag is consistent across all of the fractures, the change in the length of the surface depressions serves as a proxy for propagation rates.

## Ground-based Ice-Penetrating Radar

To characterize the vertical structure of the Daggers, we collected three terrestrial ice-penetrating radar transects during field campaigns in January 2020 and January 2023 (Figure 2). All three transects were collected on the ground, towing the instruments while walking. The 2020 transect was acquired with the Geophysical Survey Systems, Inc. (GSSI) Ground Penetrating Radar with a 100 MHz antenna. The two transects from 2023 (2023A and 2023B) were acquired with Blue Systems Integration Ltd. IceRadar system (Mingo and Flowers, 2010) with a 20 MHz antenna and Kentech Impulse Generator, which enabled a higher stacking rate during data collection than the 100 MHz system used to collect the 2020 transect.

GNSS data were collected in parallel with all radar data using a Trimble R7 antenna to determine accurate positions and were processed through the Canadian Geodetic Survey of Natural Resources Canada Precise Point Positioning application (CSRS-PPP). Elevations were then adjusted to the EGM96 Geoid (Lemoine and others, 1998), corrected for tides with the Circum-Antarctic Tidal Simulation (CATS2008)

(Padman and others, 2008), and corrected for the Inverse Barometer Effect using atmospheric pressure values from ERA5 reanalysis data (Hersbach and others, 2020).

The three radargrams were processed in a nearly identical, standard workflow using a customized version of matGPR Release 2 (Tzanis, 2010), a MATLAB®-based package for the analysis and interpretation of Ground Penetrating Radar data. The workflow consists of: 1) processing with standard techniques including dewowing, stacking, gain control, and a bandpass filter centred around the antenna frequency; 2) removing stationary traces by setting an upper bound on the cross-correlation coefficient between adjacent traces of 0.998; 3) applying a Stolt migration (Stolt, 1978); and 4) correcting for surface topography using the processed GNSS elevations. The size of the post-processing stacking window differs between the 2019 (100 MHz) and 2023 (20 MHz) workflows, as we use 10 m for the 2020 data and 2 m for the 2023 data. We present the migrated radargrams in Figures 3 and 5 d.

*2020 Transect*

The 2020 transect samples ice that had not yet been fractured by the Daggers at the time of acquisition. It is parallel to the crevasses and lies directly ahead of the tip of Crevasse 2 (Figures 2 and 5). The transect is 3.7-km-long and was collected on 06 January 2020. Crevasse 2 propagated to the beginning of the transect by July 2020. Thus, the radargram provides a snapshot of the ice-shelf structure just seven months before it fractured.

*2023 Transects*

The 2023 transects cross Crevasse 1 perpendicularly (Figure 2), providing cross-sectional profiles of the crevasse geometry (Figures 3). Transects 2023A and 2023B are 1.7-km long and were collected on January 16, 2023. Transect 2023A is located nearest to the crevasse tip, approximately 2.1 km from the tip and at 78% of the total crevasse length at the time of acquisition. Transect 2023B lies a further 1.0 km down-crevasse, closer to the origin of the crevasse, at approximately 67% of the total crevasse length. Crevasse 1 propagated to the location of transects 2023A and 2023B by the mid-2018 and early-2019, respectively. Thus, the radargrams represent a fracture that is approximately four-years old.

## Satellite-derived velocity and strain rates

To analyze changes in the dynamics of the TEIS during the formation and evolution of the Daggers, we compute annual velocity and strain rate composites with 100 m pixel size, covering the initial formation of the crevasses in 2016 and their subsequent evolution to 2026. First, we produced monthly composites using standard speckle-tracking techniques (e.g. Luckman and others, 2015) with Sentinel-1 Interferometric Wide Swath (IW) mode images. Both 6- and 12-day image pairs are included, producing monthly composite from 2–20 images, depending on image availability. A greater number of image pairs are available for months in which multiple satellites (Sentinel-1A and B or Sentinel-1A and C) acquired data. The monthly composites are then stacked and a median is taken for each pixel to produce annual composites. We note that the 2019, 2020, and 2022 annual velocity composites are biased towards summer months over our area of interest, as persistent data gaps exist in the area surrounding the Daggers (Supplementary Figure S1). The data gaps become more persistent throughout both seasons after the Sentinel-1B mission ended in 2021.

We compute changes in the flow direction of TEIS over the study period relative to a reference velocity field that is representative of the flow regime immediately prior to the formation of the Daggers. As this is beyond the temporal extent of our dataset, we use the 2014 ITS_LIVE annual composite produced by Banerjee and others (2025b). The velocity of TEIS has rotated substantially (counter-clockwise or towards true east) over the previous two decades (Alley and others, 2021), and thus, a single representative flow configuration is ambiguous. Rather, within the context of the Daggers, the 2014 reference velocity field allows us to contextualize changes in the flow direction that either favour or suppress fracture propagation.

Next, we compute surface strain rates from the annually-averaged velocity composites using the logarithmic strain rate algorithm developed by Alley and others (2018). We use a length scale of 1200 m, or approximately three ice thicknesses. This length scale is on the lower end of the expected longitudinal coupling length scale for colder ice sheets (4–10 ice thicknesses) (Cuffey and Paterson, 2010) and thus, should capture some large-scale features of the flow as well as resolve mid-scale signals associated with brittle fracture (Alley and others, 2018).

Finally, in order to maintain a constant reference frame throughout the ten-year study period, the strain rate tensor is rotated into a crevasse-oriented coordinate system aligned with the Daggers in Figure 4. Thus, positive crevasse-perpendicular strain rates indicate tensile strain across the Daggers that would promote Mode I fracturing. The crevasse-parallel direction is perpendicular to the pinning ridge, so negative strain

rates in this direction indicate compression into the pinning ridge. In order to contextualize dynamical changes with changes in the Pinning-ridge Shear Zone, we present shear strain rates in a standard flow-following coordinate system. The full time series of strain rates is presented in Supplementary Figure S2 and a representative subset is shown in Figure 4.

### Digital Elevation Models

Spatial drivers of fracture propagation are explored with two annual Digital Elevation Models (DEM) mosaics from 2020 and 2022 produced by Chartrand (2024). The DEMs were created by combining 10 m resolution strips from the Reference Elevation Model of Antarctica (REMA) into annual mosaics at 50 m resolution. The details of the methods are described by Chartrand and others (2024), including the workflows for co-registration, correcting for elevation biases with ICESat-2, CryoSat-2, and Operation IceBridge data, and masking of artifacts. The resulting elevations are converted to freeboard heights with corrections for the geoid height, mean dynamic topography, firn density, and tidal variations.

## RESULTS

### Crevasse geometry & internal structure

Radar transects 2023A and 2023B provide a cross-sectional perspective of Crevasse 1 (Figure 3), a portion of the crevasse that was approximately four years old at the time of acquisition. The map-view location of the transects is shown in Figure 2 c.

In the "younger" part of the crevasse, transect 2023A, the crevasse tip lies approximately 135 m below the surface (as resolved by the radar, Figure 3 a). Thus, the crevasse penetrated 315 m deep, or 70% of the 450-m-thick ice column. Similarly, in the "older" part of the crevasse, transect 2023B, the tip lies approximately 95 m below the surface (as resolved by the radar), penetrating 365 m deep, or 80% of the 460-m-thick ice column (Figure 3 c). In both radargrams, a 20-m-thick englacial unit of strong, discontinuous, dipping reflectors lies immediately below a bright reflector and approximately 50 m above the crevasse tip (Figure 3 b,d). Above the crevasse, the trough of the surface depression is approximately 100 m westward of the crevasse tip (Figure 3 b,d).

In transect 2023A, the crevasse width at the ice base is approximately 300 m and narrows to approximately 90 m in the middle of the shaft. The amplitude of the sidewall reflections decreases substantially in the upper 195 m of the crevasse (Figure 3 a), inhibiting further measurements of the width. In transect

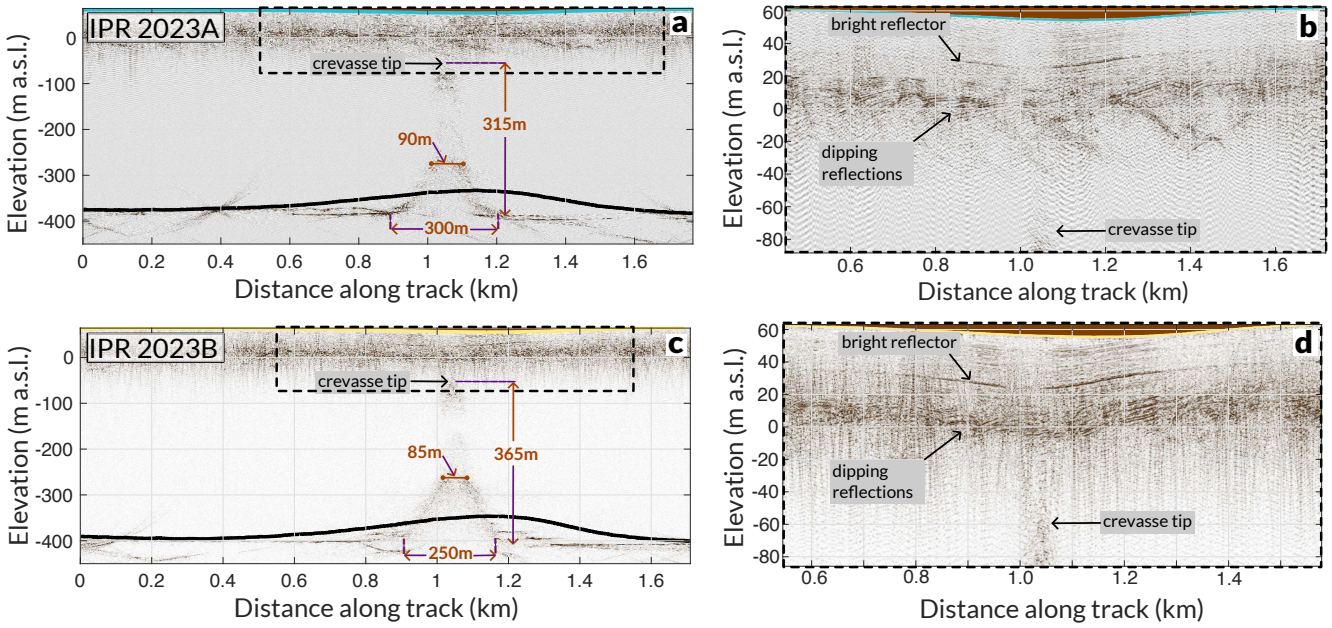



**Fig. 3. Geometry and internal structure of Crevasse 1 and the englacial layers above the crevasse tips.** (a,b) Radargram 2023A, which crosses the younger part of the crevasse closest to the crevasse tip, approximately 78% of the total crevasse length from its origin at the Pinning-ridge Shear Zone at the time of acquisition. (c,d) Radargram 2023B, crossing an older part of the crevasse, approximately 67% of its total length from its origin. The black lines in panels a and c show the theoretical bed elevation given the surface topography under the assumption of hydrostatic equilibrium. The blue and yellow lines in panels a-d denote the surface topography. Figure 2 c shows a map view of the transect tracks.

2023B, the crevasse width ranges from approximately 250 m to 85 m from the ice base to the middle of the shaft, again with a reduction in reflection amplitude in the upper 200 m (Figure 3 c). Thus, the fracture is a basal crevasse that penetrated ∼70–80% of the ice thickness with a maximum width of approximately 0.55–0.67 times the local ice thickness.

## Spatiotemporal patterns of basal crevasse propagation

In the following subsections, we contextualize the phases of fracture growth within the changing stress regime of TEIS. We identify three phases of propagation of the Daggers (Figure 2 f), connecting the timeseries of their propagation to changes in the ice-shelf dynamics: speed, flow direction, and strain rate (Figure 4). The full timeseries is presented in Supplementary Figure S2.

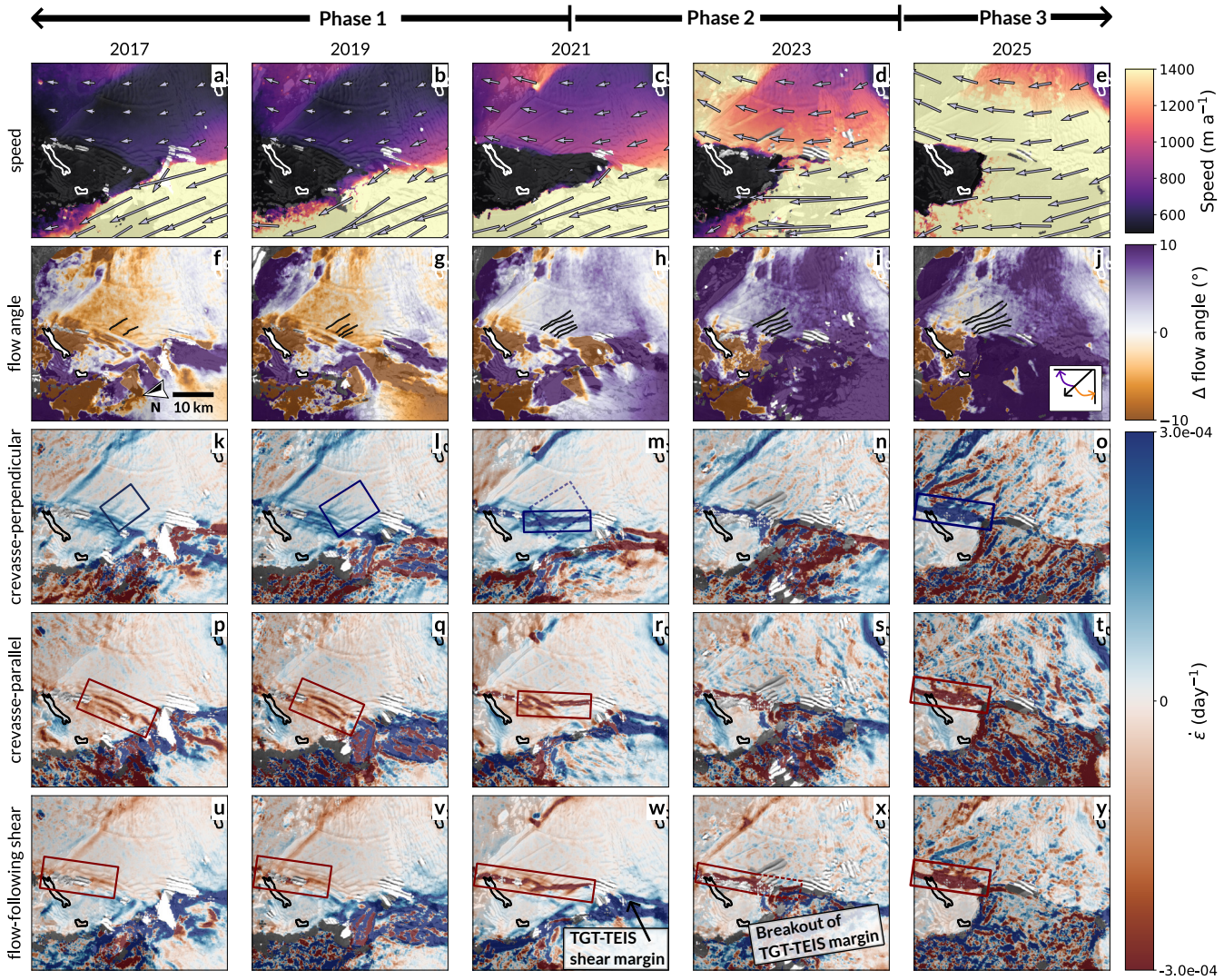



**Fig. 4. Ice flow and strain rate evolution over the lifetime of the Daggers** (a-e) Velocity magnitude and direction. (f-j) Change in ice flow direction relative to 2014 reference velocity field. Positive degrees (purple) denote clockwise rotation, i.e. turning away from the pinning ridge. Negative degrees (orange) denote counterclockwise rotation, i.e. flowing more directly into pinning ridge. Black lines denote manually-digitized crevasse traces in June of each year. (k-y) Strain rate maps derived from annual velocity composites. Normal strain rate components are shown in a coordinate system aligned with the Daggers and shear strain rates are shown in a flow-following coordinate system. Coloured boxes denote features described in text. Positive strain rates (blue) denote extension, negative strain rates (red) denote compression. Polygons (white and black) denote the 2019 pinning ridge (Wild and others, 2022).

*Phase 1 (2016 — mid-2021): Primary growth*

The primary growth phase (Phase 1) is characterized by the formation of the Daggers and their subsequent crevasse propagation to 5–8 km long (Figure 2 f).

When Crevasses 1 and 4 first appeared in the satellite imagery in 2016, the ice shelf flow is rotated counter-clockwise, striking the pinning ridge more directly than in the reference period. The flow direction reaches a maximum rotation of -5 to -7° by 2018, compared to the 2014 reference velocity field (Figure 4 f,g), and maintains this configuration until 2020, while Crevasses 3 and 5 appear and propagate. The rotation is confined to the downstream portion of the ice shelf, including the Daggers region and farther downstream towards the eastern calving front. In this flow configuration, two narrow bands of crevasse-perpendicular tensile strain on the order of $10^{-3}\,\mathrm{d}^{-1}$ extend from the Pinning-ridge Shear Zone along Crevasses 1 and 4 in 2017, 2018, and 2019 (blue boxes in Figure 4 k,l and Figure S2). A similar third band appears in 2019, following Crevasse 3 the year after it formed (blue box in Figure 4 l).

Along the Pinning-ridge Shear Zone, flow-oriented shear strain rates are higher over the eastern half of the Pinning-ridge Shear Zone than the western half (red box in Figure 4 u,v). In the western section, at the origin of the Daggers, there is crevasse-parallel compression from the pinning ridge (i.e. backstress) (red box in Figure 4 p,q). This leads to crevasse-perpendicular tensile strain over the Daggers (blue box in Figure 4 k,l).

The latter part of Phase 1 marks a transition in both crevasse propagation behaviour and the ice shelf stress regime. Between 2020 and 2021, Crevasse 2 rapidly propagated 6 km. In other words, the youngest crevasse reached the length of the oldest crevasse in a single year (Figure 2 f). At the same time, the rotation of ice flow switches from counter-clockwise to clockwise (Figure 4 g,h), the speed over the Daggers nearly doubles (Figure 4 b,c), and finally, a narrow band of shear devlops across the entire width of the Pinning-ridge Shear Zone, effectively disconnecting the ice shelf from the pinning ridge (red box in Figure 4 w, Banerjee and others, 2025b). This change in stress regime reduces the crevasse-opening stress along the Daggers, as backstress from the pinning ridge is accommodated by numerous fractures within the Pinning-ridge Shear Zone (blue box in Figure 4 m, Banerjee and others, 2025b).

*Phase 2 (mid-2021 — 2024): Quiescent period*

After five-and-a-half years of continued propagation, the growth rate of all five crevasses steadied and slowed in mid-2021 (Figure 2f), defining the beginning of the "quiescent" phase (Phase 2). During the quiescent phase, the ice shelf velocity continues to rotate clockwise, becoming nearly parallel with the Pinning-ridge Shear Zone and striking the pinning ridge more obliquely than in the primary growth phase (Phase 1). The flow rotation reaches a maximum of 7° relative to the 2014 reference velocity field over the

Daggers region (Figure 4 i), corresponding to a 12–14° rotation relative to the peak of Phase 1 (2018). The flow angle remains in this clockwise-rotated configuration between 2022–2024. Data gaps over the Daggers and noise in the 2022–2024 strain rate fields restrict our analysis of the stress regime during this period. However, we note the further narrowing and increase in magnitude of flow-oriented shear strain rates in the eastern half of the Pinning-ridge Shear Zone in 2023 (red box in Figure 4 x).

In addition to a period of flow that struck the pinning ridge more obliquely, the quiescent period coincides with two other notable events. First, by late 2021, all five crevasses reach a transition in ice geometry: a gradient from thick to thin ice, which is also the boundary of a region characterized by complex basal topography (Figure 5). The 2020 IPR transect, collected just ahead of the tip of Crevasse 2 prior to its arrival at this boundary, reveals a 130 m decrease in ice thickness over 3.5 km, with approximately 50 m of that change occurring within just 400 m (Figure 5 d). Previous IPR studies have shown that the thinner ice ahead of the crevasse tip has an undulating base overlaid with terraces and basal crevasses (Wanzer, 2025; Pettit and others, 2026). Secondly, there was a sea ice and mélange break-out in the TGT-TEIS shear margin between February and June, 2023, leaving the origin of Crevasse 5 occasionally disconnected from the Pinning-ridge Shear Zone (Figure 2 x).

*Phase 3 (2024–2026): Re-activated growth*

The quiescent phase ends in 2024, when all five crevasses propagate through the ice thickness transition and into the region of complex basal topography (Figure 2, Figure 5). Most notably, the growth rate of Crevasses 3, 4, and 5 increases to approximately 5 m $a^{-1}$ in 2025. This defines the re-activated growth phase (Phase 3), the final phase in our study period.

In 2025, the central portion of the ice shelf rotates counter-clockwise once again, flowing more directly into the pinning ridge (Figure 4 j). The 5–7° rotation is confined to the downstream portion of the ice shelf, spanning from the Daggers to the downstream eastern calving front. The flow direction in these regions is similar to 2020 (Phase 1) values (Supplementary Figure S2), with a near-0° change relative to the reference velocity direction. However, the flow direction upstream of the Daggers remains in a clockwise-rotated configuration, similar to the quiescent phase (Phase 2) velocity fields.

The final counter-clockwise rotation in 2025 is accompanied by increases in both speed and strain rates. Although noise and data gaps in the 2025 strain rate fields limit our analysis, we note the increase in all strain rate components across the entire Pinning-ridge Shear Zone (blue and red boxes in Figure 4 o,t,y).

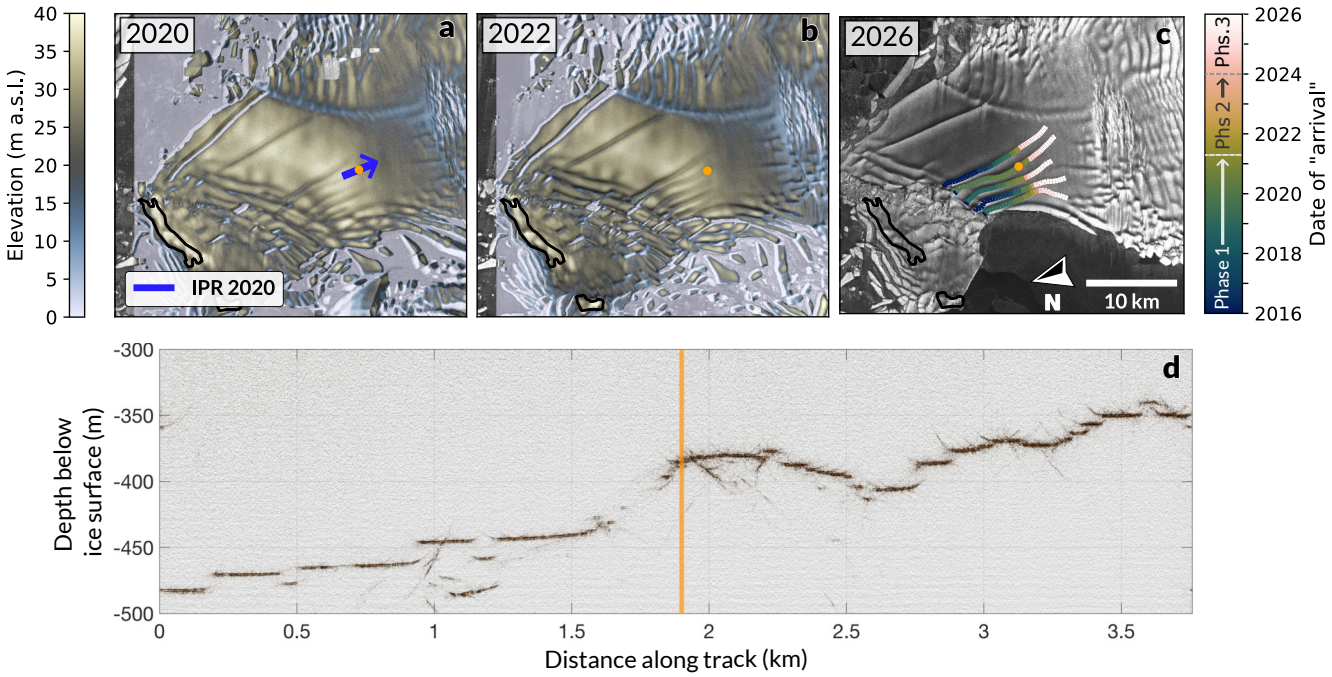



**Fig. 5. Transition in ice geometry at the tips of the Daggers during the "quiescent" phase.** Digital Elevation Models (DEMs) and radargram depicting a 130 m change in ice thickness over 3.5 km and transition to a zone of complex basal topography. (a-b) Annual DEM mosaics from Chartrand and others (2024). (c) Sentinel-1 Synthetic Aperture (SAR) base image from September 18, 2025, overlayed with manually-digitized crevasse traces. Crevasses are coloured by the date to which the tip "arrived" at each location, showing a slowing of propagation (sharp colour gradient) near the ice-geometry boundary between 2022-2025— the "quiescent" phase. The black line in panels a–c is the 2019/20 pinning ridge (Wild and others, 2022). (d) Basal topography across the geometric boundary captured from Ice-Penetrating Radar (transect location shown in panel a) that was acquired on 06 January 2020 with a 100 MHz system. The vertical orange line provides a contextual link to the orange Lagrangian reference point in panels a–c.

# DISCUSSION

## Controls on backstress-failure fracture propagation

Our results reveal three phases of backstress-failure fracture evolution on TEIS that are linked to changes in ice-flow direction and ice geometry. Relatively small ∼10° variations in flow direction drive transitions between "Dagger-favouring" and "Dagger-inhibiting" stress regimes. Here, we contextualize these flow rearrangements within a decade of weakening at the shear margins.

### *Conditions that favour propagation*

We attribute the growth of the Daggers to periods during which ice flows more directly into the pinning ridge: compressive stress due to flow into the ridge generates transverse tensile stress that favours the formation and propagation of backstress-failure fractures. During the primary growth phase (Phase 1), ice flow is oriented 12–14° more directly towards the pinning ridge than during the quiescent phase (Phase 2) (Figure 4). Similarly, during the re-activated phase (Phase 3), ice flow over the Daggers is oriented 5–10° more directly towards the pinning ridge than during the quiescent phase. This "Dagger-favouring" configuration produces crevasse-perpendicular tensile strain over the the Daggers extending from the more structurally-intact half of the Pinning-ridge Shear Zone.

The first counter-clockwise rotation that drives the propagation of the Daggers began a decade prior to their formation, in 2007, due to a weakening of the shear margin between TEIS and its neighbouring ice tongue, the Thwaites Glacier Tongue (Alley and others, 2021). With a weakened shear margin, the TEIS is no longer prevented from flowing to the west, creating a flow divergence around the pinning ridge (Alley and others, 2021; Wild and others, 2022) and numerous small rifts across the Pinning-ridge Shear Zone (Banerjee and others, 2025b). These rifts first emerged in the eastern half of the shear zone, oriented similar to the Daggers. These smaller rifts significantly reduced the resistive strength of the shear zone, establishing an east–west contrast in shear strain rates across the Pinning-ridge Shear Zone during the primary growth phase (red boxes in Figure 4 u,v). The origin of the Daggers has low shear strain rates and therefore remains compressive due to backstress from the pinning ridge (red boxes in Figure 4 p,q)—conditions favourable for the emergence of the Daggers.

A second, smaller counter-clockwise rotation occurred in 2025 (Figure 4 j), which we hypothesize is a transition to an unconfined spreading state, again controlled by its evolving margins. The rotation is

likely not driven by changes at the grounding zone, as it is confined to the downstream portion of the shelf and is accompanied by increased strain rates within the Pinning-ridge Shear Zone. The TGT-TEIS shear margin transitioned from a weak margin to a completely unconfined boundary when a landfast sea-ice breakout between February and June 2023 excavated the ice mélange within the shear margin (Figure 4 x). Model experiments from Wild and others (2022) suggest that a completely unconfined western boundary should drive counter-clockwise rotation of TEIS, a configuration representative of 2023–2025. However, a key difference between the model and the observed 2025 configuration is the shear zone upstream of the pinning ridge. With the Pinning-ridge Shear Zone developed across the entire width of the ice shelf, there is effectively no resistance from the pinning ridge and the ice shelf is able to slide along it. Thus, the ice-shelf rotation in the reactivated growth phase (Phase 3) is liekly the response to unconfined lateral boundaries and little-to-no resistance at the pinning ridge, which, in combination with continued acceleration of the entire ice shelf (Figure 4 d,e), increases ice-shelf stresses and promotes fracture propagation.

*Conditions that inhibit propagation*

The counter-clockwise rotation of ice flow and transition to unconfined spreading is briefly interrupted in 2021, when the Pinning-ridge Shear Zone weakens across the entire width of the ice shelf, but an ice mélange still occupies in the TGT-TEIS shear margin. The weakened shear zone allows ice flow to rotate clockwise and flow into the ridge at an angle (Figure 4 i). In this "Dagger-inhibiting" configuration, the propagation of the Daggers slows from over $\sim 1\,\mathrm{km\,a^{-1}}$ to less than $200\,\mathrm{m\,a^{-1}}$ (Figure 2 f). At the same time, the tips of the fractures reach a geometric boundary: a transition from thick ice with smoother basal topography to thin ice and more complex basal topography (Figure 5).

Linear Elastic Fracture Mechanics (LEFM) provides a useful conceptual framework to investigate the conditions that favour or inhibit crevasse propagation (e.g. van der Veen, 1998a,b; Hulbe and others, 2010; Luckman and others, 2012; McGrath and others, 2012). Under the assumptions of LEFM, a fracture will stop propagating once the stress at the crack tip, approximated by the stress intensity factor, falls below the fracture toughness of the material through which it is propagating. Assuming the fracture grows via Mode I opening, the stress intensity factor is proportional to the tensile stress applied normal to the crack plane (referred to as the "crevasse-opening" direction throughout this study; van der Veen, 1998b). In reality, glacier ice is not a linearly elastic material and stress can be accommodated by either ductile or brittle deformation depending on whether the strain rate falls below or exceeds the ductile-brittle transition, $\dot{\epsilon}_{db}$

(e.g. Schulson and Duval, 2009). Thus, mechanisms proposed to explain the stabilization of the Daggers during the quiescent phase (Phase 2) should either reduce the fracture-opening stress such that the strain rate falls below the ductile-to-brittle transition, increase the ductile-to-brittle transition at the fracture tips, increase the fracture toughness of the ice, or a combination of these. We propose three possible explanations:

1. a reduction in tensile crevasse-opening stress caused by the clockwise rotation of ice flow, and/or
2. a change in the ductile-to-brittle transition strain rate at the geometrical boundary due to the change in ice thickness, and/or
3. a change in fracture toughness at the geometrical boundary due to material heterogeneity.

Because these processes occurred at the same time, their individual contributions cannot be isolated from observations alone. With this limitation, we only speculate on (1) and (3) and explore (2) using an idealized numerical experiment.

*Hypothesis 1. Reduction in crevasse-opening stress caused by the clockwise rotation of ice flow:*

When the Pinning-ridge Shear Zone developed across the entire width of the ice shelf, it connected with the TGT-TEIS shear margin (red box in Figure 4 w and Supplementary Figure S2) and acted as a boundary for ice flow. Thus, the flow rotated clockwise to follow this boundary, striking the pinning ridge at a more oblique angle. This change in flow angle would theoretically reduce the crevasse-opening stress over the Daggers, but data gaps in the strain rate maps during this period limit direct observation (Figure 4 n). Additionally, backstress from the pinning ridge was accommodated by fractures within the Pinning-ridge Shear Zone (red and blue boxes in Figure 4 m,r,w), effectively decoupling the pinning ridge from the rest of the ice shelf. This could also contribute to reduced crevasse-opening stress over the Daggers (dashed box in Figure 4 m).

*Hypothesis 2. Change in the ductile-to-brittle transition strain rate at the geometrical boundary due to the change in ice thickness:*

We explore the effect of the change in ice thickness on the stress state at the fracture tips with a simple, idealized experiment in the finite-element glacier flow modelling package *icepack* (Shapero and others, 2021). We solve the diagnostic Shallow Shelf Approximation (SSA) over a synthetic two-dimensional domain

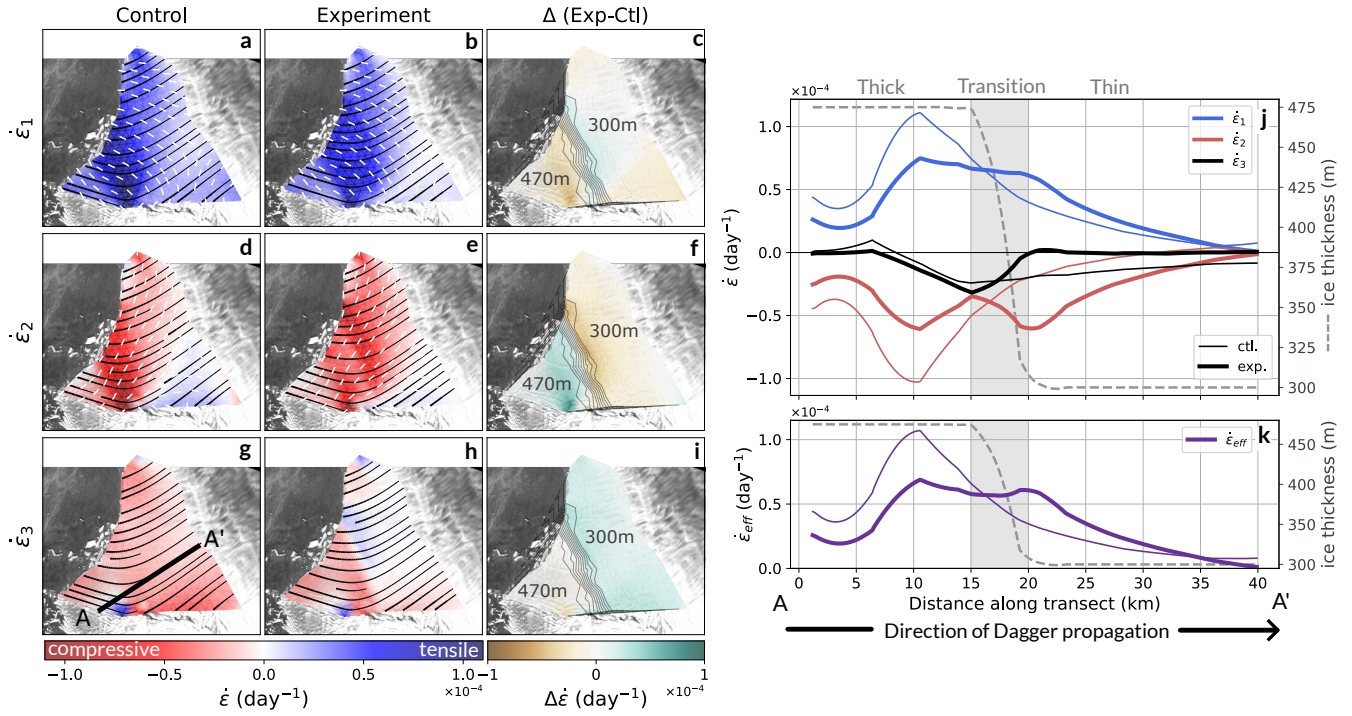



**Fig. 6. Change in stress regime across an idealized ice-thickness transition**. Model results overlaid on a Sentinel-1 image of TEIS acquired on June 15, 2018. (a,b) Direction (white lines) of the first principal direction ($\dot{\epsilon}_1$) and magnitude of corresponding strain rate for the control with uniform ice thickness (a) and the experiment with an ice-thickness gradient (b). Negative denotes compression and positive denotes extension. Velocity streamlines are shown in black. Note that $\dot{\epsilon}_1$ is the "crevasse-opening" direction. (d,e) Same as a and b but for the second principal direction ($\dot{\epsilon}_2$). (g,h) Same as a and b but for the vertical principal direction ($\dot{\epsilon}_3$). (c,f,i) Difference in the magnitude of the principal strain rates between the control and experiment solution. Grey lines denote 20 m ice thickness contours. (j) Transect of principal strain rates for the control (thin line) and experiment (thick line) simulations along the profile shown in panel g, the approximate trajectory of the Daggers. The ice thickness along the profile is shown in grey. The shaded region highlights the transition between thick and thin ice. (k) Same as j but for the effective strain rate ($\dot{\epsilon}_{eff}$).

representing TEIS in the later part of the study period, similar to its 2021-2023 configuration (Figure 6). We assume a constant rate factor across the domain for a temperature of -18°C. The TGT–TEIS shear-margin and the eastern terminus are treated as ice fronts subject only to hydrostatic seawater pressure. At the upstream grounding line, we impose a constant inflow of $\sim 860$ m a$^{-1}$. At the downstream boundary, the Pinning-ridge Shear Zone is modelled as a frictional side wall with a mixed Dirichlet–Robin condition: ice cannot flow through the boundary ($\mathbf{u} \cdot \mathbf{n} = 0$), while tangentially, ice can slide along the boundary with a given friction coefficient (Shapero and others, 2021). In our simulations, friction along the downstream side wall is held constant with a coefficient of 0.01, which provides negligible resistance to flow (Miele and others, 2023). In reality, ice is able to flow through the Pinning-ridge Shear Zone, however, we argue that this is a reasonable representation of the boundary from 2021 onwards, when the ice flux through the shear zone is very small (Figure 4 c,d,e).

We solve the diagnostic equation for both a control solution with uniform ice thickness (475 m) and an experimental solution with a sigmoidal thickness change from 300 m to 475 m over 3.5 km (Figure 6), a simplified representation of the observed ice geometry (Figure 5). The modelled principal strain rates are shown in Figure 6 a–i. Figure 6 j shows a profile of the strain rate components along an approximate trajectory of the Daggers. We assume incompressibility to calculate the vertical principal strain rate: $\dot{\epsilon}_3 = -(\dot{\epsilon}_1 + \dot{\epsilon}_2)$. For an isotropic material, we can use spatial patterns in strain rate as a proxy for spatial patterns in deviatoric stress. Because ice is a viscous material, we also calculate the effective strain rate (second invariant of the strain rate tensor, Figure 6 k) as a proxy for effective stress, which modulates the viscosity of the ice in our constant-temperature model.

The constant-thickness (control) case shows a peak in modelled horizontal stresses approximately 10 km from the sidewall boundary (model representation of the Pinning-ridge Shear Zone), which then gradually decreases with distance (Figure 6 j). The vertical strain rate shows overall thinning, as expected for ice shelf spreading, with the maximum thinning rates in the middle, far from the imposed boundary conditions at the pinning ridge and grounding zone (Figure 6 g,j). The specific locations of these peak stresses relate to the shape of the domain and the boundary conditions, so our analysis is focused on their spatial variation, rather than the absolute locations. Under these stress conditions and LEFM assumptions, the Daggers would stop propagating when the crack-opening stress (represented by $\dot{\epsilon}_1$) drops below the fracture toughness.

For the model run with variable ice thickness, the stress pattern shows a similar initial increase with

distance from the Pinning-ridge Shear Zone, followed by a decrease along the trajectory of the Daggers (Figure 6 j). One key difference in the stress conditions is that the vertical thinning due to ice shelf spreading (the thick black curve in Figure 6 j, $\dot{\epsilon}_3$) is concentrated in the thick ice because the gravitational driving stress is higher in thick ice. This shifts the stress distribution such that the peak in each component is lower and broader, with the subsequent gradual decrease in stress magnitudes appearing beyond the thickness transition (the grey shading in Figure 6 j,k).

This pattern of stress leads to two observations. First the crevasse-opening principal stress is higher near the location where the Dagger tips stopped propagating (Figure 6 j), which is the opposite of what would be expected to inhibit Dagger propagation. Second, the effective stress (proxied by the effective strain rate in Figure 6 k) is significantly higher (by $\sim 10^{-5}$ day$^{-1}$) than in the control case at the transition to thinner ice. This increase in effective stress would lead to a softening of the ice at this transition, given the stress-dependent viscosity of ice. Thus, the experiments suggest that all components of the stress tensor may be important controls on fracture propagation, not just the Mode I opening stress.

One plausible explanation that accounts for all stress components is a change in the ductile-to-brittle transition due to the increase in effective stress at ice-thickness boundary. The threshold strain rate at which ice switches from ductile deformation to brittle deformation ($\dot{\epsilon}_{db}$) can be expressed as

$$\dot{\epsilon}_{db} = A\, K_{Ic}^{n}\, (\lambda d)^{-n/2} \tag{1}$$

where A is the flow-rate factor, $K_{Ic}$ is the Mode I fracture toughness, n is the flow-law exponent, $\lambda$ is a numerical factor that relates crack size to grain size, and d is the grain size (Schulson and Duval, 2009, Equation 10.5). However, this equation was derived considering only the crevasse-perpendicular Mode I opening stress. As discussed above, considering all stress components leads to an increase in effective stress at the transition to thinner ice, and therefore a decrease in ice viscosity. This could essentially be accounted for by increasing the ice softness through A in Equation 1, ultimately increasing $\dot{\epsilon}_{db}$.

Thus, the softer ice at the ice-thickness transition may accommodate stresses viscously instead of brittlely, and inhibit fracture propagation during the quiescent phase. That is, until the effective strain rate increases to the elevated ductile–brittle threshold and the fractures propagate through the transition to thinner ice. Once the fractures reach the thin ice, the effective stress continues to decrease (Figure 6 k) and the thin ice itself would not pose a barrier to further propagation. An advantage of this hypothesis is its ability to explain the re-activation of the Daggers.

All in all, we argue that fracture behaviour is sensitive to changes in any/all of the stress components due to the nonlinear rheology and stress-dependent viscosity of ice—a mechanism not captured in the LEFM framework. Future theoretical and observational work could test the hypotheses laid out here, and may include the full complexity of the observed base geometry, including undulations, basal terraces, and existing basal crevasses (Wanzer, 2025; Pettit and others, 2026), which are not captured in our model.

*Hypothesis 3. Change in fracture toughness at the geometrical boundary due to material heterogeneity:* Our simple model does not consider material heterogeneity at this boundary, which is a well-known cause of fracture termination in suture zones (e.g. Hulbe and others, 2010; McGrath and others, 2014; Borstad and others, 2017). Despite being regions of thin ice, suture zones are considered "stronger" than neighbouring ice due to their higher fracture toughness. The complexity of basal topography in the thin-ice zone and the presence of terraces and basal crevasses immediately upstream of our study site (Wanzer, 2025; Pettit and others, 2026) may imply that it has experienced more strain than the thick-ice region, which could have changed the material properties and fracture toughness, analogous to a suture zone.

## Insights on vertical crevasse propagation

While the horizontal propagation of the Daggers is largely driven by weakening of the ice-shelf margins, the controls on their vertical propagation are less clear. In particular, we question why these large basal crevasses did not develop into full-thickness rifts along most of the fracture, in contrast to backstress-failure fractures on the Conger-Glenzer and Wilkins ice shelves (Figure 1).

The radargrams reveal an englacial unit of dipping reflectors immediately below a continuous bright reflector and 50 m above the crevasse tip (Figure 3 b&d). We interpret the continuous bright reflector as a layer that formed due to enhanced melt, possibly at the grounding zone. Katabatic winds originating from the interior of the ice sheet have been shown to warm and mix air as they descend down steep surface gradients towards the grounding lines of ice shelves, creating enhanced and prolonged melt at the grounding line (Lenaerts and others, 2017; Saunderson and others, 2022) that may create such a bright reflector. It is plausible, then, that the unit of dipping layers formed due to deformation in the grounding zone, similar to those observed in Miles and others (2025).

Regardless of its source, these observations suggest that a change in rheological properties that affects the fracture toughness could limit vertical crevasse penetration. Dampening of vertical fracture propagation

when it encounters ice of different properties would again be analogous to the dampening of horizontal propagation as rifts cross suture zones (e.g. Hulbe and others, 2010; McGrath and others, 2014; Borstad and others, 2017). Thus, inherited heterogeneity in the vertical rheological structure of ice shelves may be an important control on basal crevasse penetration depths.

## A comparison of backstress-failure fractures across ice shelves and their role in ice-shelf breakup

The Wordie, Wilkins, and Conger-Glenzer ice shelves all exhibit fractures that extend orthogonally upstream from their pinning points, similar to the Daggers, in the decade(s) leading up to their final collapse. The role of the Daggers in the breakup of TEIS differs slightly, but crucially, from those previously observed cases.

During the breakup of the Wordie Ice Shelf, the three major ice rises that once stabilized the ice shelf aided in its destruction as large longitudinal rifts propagated directly upstream. These rifts eventually led to calving and unpinning (Figure 1; Doake and Vaughan, 1991; Dømgaard and others, 2025). On the Wilkins Ice Shelf, two pairs of parallel fractures extended upstream from an ice rise (Charcot Island): one pair formed simultaneous to or shortly after a 1998 breakup event and the other pair preceded the 2008 breakup events (Braun and others, 2009). Similarly, on the Conger–Glenzer Ice Shelf, the final stage of breakup was characterized by tabular iceberg calving along large tensile rifts—at least one of which extended from its pinning point into the main body of the ice shelf (Figure 1)—as ice flow changed direction to divert around the island (Walker and others, 2024). In all of these cases, the backstress-failure fractures calved into tabular icebergs on timescales of a few years to a decade.

A key difference between the dynamics of TEIS and these ice shelves, however, is the development of a shear zone along its pinning ridge. Benn and others (2022) show that pre-existing damage is required to develop the shear zone observed on TEIS, likely due to the significant backstress it experienced while it was coupled with the Thwaites Glacier Tongue (Alley and others, 2021). In contrast, the Wordie, Wilkins, and Conger–Glenzer ice shelves did not develop shear zones, likely because they lacked sufficient pre-existing damage at their pinning points. Instead, they formed large fractures similar to the Daggers that propagate upstream from their pinning points. In this study, we show that the development of the Pinning-ridge Shear Zone plays an important role in inhibiting the growth of the Daggers during the quiescent phase. From this perspective, the shear zone may have briefly stabilized—and possibly prolonged—the ice shelf

by reducing the backstress and corresponding tensile crevasse-opening stress of the Daggers. Rather than breaking up via large calving events along the Daggers, TEIS now slides along the Pinning-ridge Shear Zone and occasionally calves at its margins. However, we hypothesize that the Daggers will ultimately form tabular icebergs in the final collapse of TEIS.

## CONCLUSION

In this study, we used a combination of field-based and satellite data to investigate the controls on the horizontal and vertical propagation of fractures emanating from the pinning ridge on TEIS, which we categorize as *backstress-failure fractures*. We identify three phases of fracture propagation, from their initial growth to a two-and-a-half-year quiescent phase, and finally, a re-activation. These phases are associated with fluctuations in the direction of ice flow on the order of $\sim$10°, largely in response to changes at the pinning-ridge margin. Configurations in which ice flows more directly into the pinning ridge create stresses favourable for fracture propagation. Conversely, the development of a shear zone has effectively disconnected the ice shelf from its pinning ridge and, may have temporarily stabilized the fractures. We also show that a change effective stress at the fracture tips due to a transition from thick to thin ice could have inhibited fracture propagation by increasing the ductile-to-brittle transition strain rate, but additional modelling is required to further test this hypothesis. This highlights the sensitivity of fracture propagation to the transient-nature of stresses during backstress-triggered ice-shelf breakup. At the time of writing, the Daggers continue to propagate across the ice shelf.

We also explore controls on vertical crevasse propagation with ground-based ice-penetrating radar across one of the crevasses, revealing the fracture geometry: a basal crevasse that penetrates $\sim$70–80% of the ice column with a maximum width comparable to the ice thickness. We observe an englacial unit of dipping reflectors directly above the crevasse tip, which we hypothesize is a change in material properties and possibly, a change in fracture toughness that could have limited the height of crevasse penetration. This observation highlights the potential role of inherited rheological properties on ice-shelf stability, and motivates further investigations on how and when these heterogeneous material properties impact the penetration of basal crevasses.

Overall, the role of pinning points in ice-shelf *de*stabilization has been overlooked until recently, motivating the need to re-evaluate their influence on fracture propagation, both in observations of past breakup events and in projections of future change. Our results suggest that backstress-failure fractures, such as

the Daggers, may be an easily-observable indicator that pinning-point-driven destabilization is underway and could provide a promising avenue towards a new collapse criterion in ice-sheet models.

## ACKNOWLEDGEMENTS

This work is from the TARSAN project, a component of the International Thwaites Glacier Collaboration (ITGC). Support from National Science Foundation (NSF: Grant 1929991) and Natural Environment Research Council (NERC: Grant NE/S006419/1). Logistics provided by NSF-U.S. Antarctic Program and NERC-British Antarctic Survey. ITGC Contribution No. ITGC-176. MAS was partially supported by the Canada Graduate Research Scholarship– Doctoral (CGRS D) from the Natural Sciences and Engineering Research Council of Canada (NSERC). CTW was partially supported by the Deutsche Forschungsgemeinschaft (DFG) in the framework of the priority programme 1158 'Antarctic Research with comparative investigations in Arctic ice areas' by a grant (DR 822/8-1).

We thank all members of the TARSAN project for their ideas, contributions, and thought-provoking discussions through the years that helped shaped this project. Specifically, we thank field team members Michelle L. Maclennan, Naomi Ochwat, Gabi Collao-Barrios, Emelie Mahdavian, and Cecelia Mortenson for their support in collecting the radar data and endless exciting discussions about The Daggers. We also thank the Kenn Borek Air and WAIS Divide teams for making this fieldwork possible. Finally, we thank Zoee K Beiergrohslein for her help in digitizing the fractures and the entire Glaciology Research Team at Oregon State University for their ideas along the way.

## DATA AVAILABILITY

Sentinel-1 images used to digitized the fractures in this study are freely available from the Copernicus Open Access Hub (https://scihub.copernicus.eu/). The manually-digitized fracture shapefiles (doi:*TBD upon acceptance*), ice-penetrating radar data (doi:*TBD upon acceptance*), and monthly and annual velocity composites and annual strain rates (doi:*TBD upon acceptance*) are all hosted on the U.S. Antarctic Program Data Center (USAP-DC). Code to compute the strain rates from the velocity composites can be can be found in the supplementary material of Alley and others (2018). The 2014 reference velocity used in this study can be downloaded from (Banerjee and others, 2025a). Digital Elevation Models can be downloaded from (Chartrand, 2024). The open-source *icepack* library (Shapero and others, 2021) is hosted on GitHub (https://github.com/icepack/icepack), and our code to reproduce the model experiments in this study and

Figure 6 can be downloaded from Zenodo (doi:*TBD upon acceptance*).

## AI DECLARATION

Artificial Intelligence (AI) and AI-assisted technologies were used during the research processes to debug code, specifically to produce author-defined figure layouts and aesthetics using ChatGPT and Claude Sonnet 5. In the writing process, ChatGPT and Grammarly were used to assist with grammar, spelling, and sentence structure. AI was not used to generate ideas, analyze or extract insights from data, nor to generate original text or images for this paper.

## REFERENCES

Alley KE, Scambos TA, Anderson RS, Rajaram H, Pope A and Haran TM (2018) Continent-wide estimates of Antarctic strain rates from Landsat 8-derived velocity grids. *Journal of Glaciology*, **64**(244), 321–332, ISSN 0022-1430, 1727-5652 (doi: 10.1017/jog.2018.23)

Alley KE, Wild CT, Luckman A, Scambos TA, Truffer M, Pettit EC, Muto A, Wallin B, Klinger M, Sutterley T, Child SF, Hulen C, Lenaerts JTM, Maclennan M, Keenan E and Dunmire D (2021) Two decades of dynamic change and progressive destabilization on the Thwaites Eastern Ice Shelf. *The Cryosphere*, **15**(11), 5187–5203, ISSN 1994-0416 (doi: 10.5194/tc-15-5187-2021)

Alley KE, Washam P, Alley RB, Benn DI, Kulessa B, Luckman A, Muto A, Pettit E, Scambos TA, Truffer M and Wild CT (in review) Ice-Shelf Collapse: A Long Time Coming. *Science Advances*

Arthur JF, Hogg AE, Miles BWJ, Walker CC and Wallis BJ (2026) Reconsidering the drivers of ice-shelf collapse. *Nature Communications*, ISSN 2041-1723 (doi: 10.1038/s41467-026-76772-1)

Åström J and Benn D (2019) Effective Rheology Across the Fragmentation Transition for Sea Ice and Ice Shelves. *Geophysical Research Letters*, **46**(22), 13099–13106, ISSN 1944-8007 (doi: 10.1029/2019GL084896)

Bamber JL, Riva REM, Vermeersen BLA and LeBrocq AM (2009) Reassessment of the Potential Sea-Level Rise from a Collapse of the West Antarctic Ice Sheet. *Science*, **324**(5929), 901–903 (doi: 10.1126/science.1169335)

Banerjee D, Alley K, Lilien D, Luckman A, Muto A, Pettit EC, Scambos T, Truffer M and Wild C (2025a) Yearly velocity and strain-rate averages from the Thwaites Eastern Ice Shelf, 2013-2022 (doi: 10.15784/601904)

Banerjee D, Lilien DA, Truffer M, Luckman A, Wild CT, Pettit EC, Scambos TA, Muto A and Alley KE (2025b) Evolution of Shear-Zone Fractures Presages the Disintegration of Thwaites Eastern Ice Shelf. *Journal of Geophysical Research: Earth Surface*, **130**(9), e2025JF008352, ISSN 2169-9011 (doi: 10.1029/2025JF008352)

Barnes JM, Gudmundsson GH, Goldberg DN and Sun S (2026) Modelling the sensitivity of ice loss to calving front retreat rates in the Amundsen Sea Embayment, West Antarctica. *The Cryosphere*, **20**(1), 777–790, ISSN 1994-0416 (doi: 10.5194/tc-20-777-2026)

Bassis JN and Ma Y (2015) Evolution of basal crevasses links ice shelf stability to ocean forcing. *Earth and Planetary Science Letters*, **409**, 203–211, ISSN 0012-821X (doi: 10.1016/j.epsl.2014.11.003)

Benn DI, Luckman A, Åström JA, Crawford AJ, Cornford SL, Bevan SL, Zwinger T, Gladstone R, Alley K, Pettit E and Bassis J (2022) Rapid fragmentation of Thwaites Eastern Ice Shelf. *The Cryosphere*, **16**(6), 2545–2564, ISSN 1994-0416 (doi: 10.5194/tc-16-2545-2022)

Borstad C, McGrath D and Pope A (2017) Fracture propagation and stability of ice shelves governed by ice shelf heterogeneity. *Geophysical Research Letters*, **44**(9), 4186–4194, ISSN 1944-8007 (doi: 10.1002/2017GL072648)

Braun M and Humbert A (2009) Recent Retreat of Wilkins Ice Shelf Reveals New Insights in Ice Shelf Breakup Mechanisms. *IEEE Geoscience and Remote Sensing Letters*, **6**(2), 263–267, ISSN 1558-0571 (doi: 10.1109/LGRS.2008.2011925)

Braun M, Humbert A and Moll A (2009) Changes of Wilkins Ice Shelf over the past 15 years and inferences on its stability. *The Cryosphere*, **3**(1), 41–56, ISSN 1994-0416 (doi: 10.5194/tc-3-41-2009)

Burgard C, Jourdain NC, Mosbeux C, Caillet J, Mathiot P and Kittel C (2025) Ocean warming threatens the viability of 60% of Antarctic ice shelves. *Nature*, **647**(8088), 102–108, ISSN 1476-4687 (doi: 10.1038/s41586-025-09657-w)

Chartrand A (2024) Thwaites Glacier thins and retreats fastest where ice-shelf channels intersect its grounding zone, dataset+code (doi: 10.5281/zenodo.13667120)

Chartrand AM, Howat IM, Joughin IR and Smith BE (2024) Thwaites Glacier thins and retreats fastest where ice-shelf channels intersect its grounding zone. *The Cryosphere*, **18**(11), 4971–4992, ISSN 1994-0416 (doi: 10.5194/tc-18-4971-2024)

Cuffey K and Paterson WSB (2010) *The Physics of Glaciers*. Book, Whole, Academic Press, Burlington, MA, 4 edition, ISBN 0123694612;9780123694614;

Doake CSM and Vaughan DG (1991) Rapid disintegration of the Wordie Ice Shelf in response to atmospheric warming. *Nature*, **350**(6316), 328–330, ISSN 1476-4687 (doi: 10.1038/350328a0)

Dømgaard M, Millan R, Andersen JK, Scheuchl B, Rignot E, Izeboud M, Bernat M and Bjørk AA (2025) Half a century of dynamic instability following the ocean-driven break-up of Wordie Ice Shelf. *Nature Communications*, **16**(1), 4016, ISSN 2041-1723 (doi: 10.1038/s41467-025-59293-1)

dos Santos TD, Barnes JM, Goldberg DN, Gudmundsson GH and Morlighem M (2021) Drivers of Change of Thwaites Glacier, West Antarctica, Between 1995 and 2015. *Geophysical Research Letters*, **48**(20), e2021GL093102, ISSN 1944-8007 (doi: 10.1029/2021GL093102)

Dunmire D, Wever N, Banwell AF and Lenaerts JTM (2024) Antarctic-wide ice-shelf firn emulation reveals robust future firn air depletion signal for the Antarctic Peninsula. *Communications Earth & Environment*, **5**(1), 100, ISSN 2662-4435 (doi: 10.1038/s43247-024-01255-4)

Dutrieux P, De Rydt J, Jenkins A, Holland PR, Ha HK, Lee SH, Steig EJ, Ding Q, Abrahamsen EP and Schröder M (2014) Strong Sensitivity of Pine Island Ice-Shelf Melting to Climatic Variability. *Science*, **343**(6167), 174–178 (doi: 10.1126/science.1244341)

Hersbach H, Bell B, Berrisford P, Hirahara S, Horányi A, Muñoz-Sabater J, Nicolas J, Peubey C, Radu R, Schepers D, Simmons A, Soci C, Abdalla S, Abellan X, Balsamo G, Bechtold P, Biavati G, Bidlot J, Bonavita M, De Chiara G, Dahlgren P, Dee D, Diamantakis M, Dragani R, Flemming J, Forbes R, Fuentes M, Geer A, Haimberger L, Healy S, Hogan RJ, Hólm E, Janisková M, Keeley S, Laloyaux P, Lopez P, Lupu C, Radnoti G, de Rosnay P, Rozum I, Vamborg F, Villaume S and Thépaut JN (2020) The ERA5 global reanalysis. *Quarterly Journal of the Royal Meteorological Society*, **146**(730), 1999–2049, ISSN 1477-870X (doi: 10.1002/qj.3803)

Holland PR, Bracegirdle TJ, Dutrieux P, Jenkins A and Steig EJ (2019) West Antarctic ice loss influenced by internal climate variability and anthropogenic forcing. *Nature Geoscience*, **12**(9), 718–724, ISSN 1752-0908 (doi: 10.1038/s41561-019-0420-9)

Hulbe CL, LeDoux C and Cruikshank K (2010) Propagation of long fractures in the Ronne Ice Shelf, Antarctica, investigated using a numerical model of fracture propagation. *Journal of Glaciology*, **56**(197), 459–472, ISSN 0022-1430, 1727-5652 (doi: 10.3189/002214310792447743)

Jacobs SS, Jenkins A, Giulivi CF and Dutrieux P (2011) Stronger ocean circulation and increased melting under Pine Island Glacier ice shelf. *Nature Geoscience*, **4**(8), 519–523, ISSN 1752-0908 (doi: 10.1038/ngeo1188)

Joughin I, Smith BE and Medley B (2014) Marine Ice Sheet Collapse Potentially Under Way for the Thwaites Glacier Basin, West Antarctica. *Science*, **344**(6185), 735–738 (doi: 10.1126/science.1249055)

Lemoine FG, Kenyon SC, Factor JK, Trimmer RG, Pavlis NK, Chinn DS, Cox CM, Klosko SM, Luthcke SB, Torrence MH, Wang YM, Williamson RG, Pavlis EC, Rapp RH and Olson TR (1998) The Development of the Joint NASA GSFC and the National Imagery and Mapping Agency (NIMA) Geopotential Model EGM96

Lenaerts JTM, Lhermitte S, Drews R, Ligtenberg SRM, Berger S, Helm V, Smeets CJPP, van den Broeke MR, van de Berg WJ, van Meijgaard E, Eijkelboom M, Eisen O and Pattyn F (2017) Meltwater produced by wind–

albedo interaction stored in an East Antarctic ice shelf. *Nature Climate Change*, **7**(1), 58–62, ISSN 1758-6798 (doi: 10.1038/nclimate3180)

Lhermitte S, Sun S, Shuman C, Wouters B, Pattyn F, Wuite J, Berthier E and Nagler T (2020) Damage accelerates ice shelf instability and mass loss in Amundsen Sea Embayment. *Proceedings of the National Academy of Sciences*, **117**(40), 24735–24741 (doi: 10.1073/pnas.1912890117)

Luckman A, Jansen D, Kulessa B, King EC, Sammonds P and Benn DI (2012) Basal crevasses in Larsen C Ice Shelf and implications for their global abundance. *The Cryosphere*, **6**(1), 113–123, ISSN 1994-0416 (doi: 10.5194/tc-6-113-2012)

Luckman A, Benn DI, Cottier F, Bevan S, Nilsen F and Inall M (2015) Calving rates at tidewater glaciers vary strongly with ocean temperature. *Nature Communications*, **6**(1), 8566, ISSN 2041-1723 (doi: 10.1038/ncomms9566)

McGrath D, Steffen K, Scambos T, Rajaram H, Casassa G and Lagos JLR (2012) Basal crevasses and associated surface crevassing on the Larsen C ice shelf, Antarctica, and their role in ice-shelf instability. *Annals of Glaciology*, **53**(60), 10–18, ISSN 0260-3055, 1727-5644 (doi: 10.3189/2012AoG60A005)

McGrath D, Steffen K, Holland PR, Scambos T, Rajaram H, Abdalati W and Rignot E (2014) The structure and effect of suture zones in the Larsen C Ice Shelf, Antarctica. *Journal of Geophysical Research: Earth Surface*, **119**(3), 588–602, ISSN 2169-9011 (doi: 10.1002/2013JF002935)

Miele C, Bartholomaus TC and Enderlin EM (2023) Marginal Detachment Zones: The Fracture Factories of Ice Shelves? *Journal of Geophysical Research: Earth Surface*, **128**(6), e2022JF006959, ISSN 2169-9011 (doi: 10.1029/2022JF006959)

Miles BWJ, Stokes CR, Jenkins A, Jordan JR, Jamieson SSR and Gudmundsson GH (2020) Intermittent structural weakening and acceleration of the Thwaites Glacier Tongue between 2000 and 2018. *Journal of Glaciology*, **66**(257), 485–495, ISSN 0022-1430, 1727-5652 (doi: 10.1017/jog.2020.20)

Miles KE, Hubbard B, Luckman A, Kulessa B, Bevan S, Thompson S and Jones G (2025) Influence of the grounding zone on the internal structure of ice shelves. *Nature Communications*, **16**(1), 4383, ISSN 2041-1723 (doi: 10.1038/s41467-025-58973-2)

Mingo L and Flowers GE (2010) An integrated lightweight ice-penetrating radar system. *Journal of Glaciology*, **56**(198), 709–714, ISSN 0022-1430, 1727-5652 (doi: 10.3189/002214310793146179)

Morlighem M, Rignot E, Binder T, Blankenship D, Drews R, Eagles G, Eisen O, Ferraccioli F, Forsberg R, Fretwell P, Goel V, Greenbaum JS, Gudmundsson H, Guo J, Helm V, Hofstede C, Howat I, Humbert A, Jokat W, Karlsson NB, Lee WS, Matsuoka K, Millan R, Mouginot J, Paden J, Pattyn F, Roberts J, Rosier S, Ruppel A, Seroussi H,

Smith EC, Steinhage D, Sun B, van den Broeke MR, van Ommen TD, van Wessem M and Young DA (2020) Deep glacial troughs and stabilizing ridges unveiled beneath the margins of the Antarctic ice sheet. *Nature Geoscience*, **13**(2), 132–137, ISSN 1752-0908 (doi: 10.1038/s41561-019-0510-8)

Padman L, Erofeeva SY and Fricker HA (2008) Improving Antarctic tide models by assimilation of ICESat laser altimetry over ice shelves. *Geophysical Research Letters*, **35**(22), ISSN 1944-8007 (doi: 10.1029/2008GL035592)

Pettit EC, Sauret G, Wanzer L, Alley KE, Zhao K, Maclennan M, Truffer M, Sharp MA, Wahlin A and Wild C (2026) The complex undersides of ice shelves: Interplay of ocean circulation, ice shape, melt patterns, ice flow, and fracture. In *American Geophysical Union, Ocean Sciences Meeting*, HE41A–04

Rignot E, Mouginot J, Morlighem M, Seroussi H and Scheuchl B (2014) Widespread, rapid grounding line retreat of Pine Island, Thwaites, Smith, and Kohler glaciers, West Antarctica, from 1992 to 2011. *Geophysical Research Letters*, **41**(10), 3502–3509, ISSN 1944-8007 (doi: 10.1002/2014GL060140)

Rott H, Rack W, Nagler T and Skvarca P (1998) Climatically induced retreat and collapse of northern Larsen Ice Shelf, Antarctic Peninsula. *Annals of Glaciology*, **27**, 86–92, ISSN 0260-3055, 1727-5644 (doi: 10.3189/S0260305500017262)

Saunderson D, Mackintosh A, McCormack F, Jones RS and Picard G (2022) Surface melt on the Shackleton Ice Shelf, East Antarctica (2003–2021). *The Cryosphere*, **16**(10), 4553–4569, ISSN 1994-0416 (doi: 10.5194/tc-16-4553-2022)

Scambos T, Hulbe C and Fahnestock M (2003) Climate-Induced Ice Shelf Disintegration in the Antarctic Peninsula. In *Antarctic Peninsula Climate Variability: Historical and Paleoenvironmental Perspectives*, 79–92, American Geophysical Union (AGU), ISBN 978-1-118-66845-0 (doi: 10.1029/AR079p0079)

Scambos T, Fricker HA, Liu CC, Bohlander J, Fastook J, Sargent A, Massom R and Wu AM (2009) Ice shelf disintegration by plate bending and hydro-fracture: Satellite observations and model results of the 2008 Wilkins ice shelf break-ups. *Earth and Planetary Science Letters*, **280**(1), 51–60, ISSN 0012-821X (doi: 10.1016/j.epsl.2008.12.027)

Scambos TA, Hulbe C, Fahnestock M and Bohlander J (2000) The link between climate warming and break-up of ice shelves in the Antarctic Peninsula. *Journal of Glaciology*, **46**(154), 516–530, ISSN 0022-1430, 1727-5652 (doi: 10.3189/172756500781833043)

Scambos TA, Bell RE, Alley RB, Anandakrishnan S, Bromwich DH, Brunt K, Christianson K, Creyts T, Das SB, DeConto R, Dutrieux P, Fricker HA, Holland D, MacGregor J, Medley B, Nicolas JP, Pollard D, Siegfried MR, Smith AM, Steig EJ, Trusel LD, Vaughan DG and Yager PL (2017) How much, how fast?: A science review and outlook for research on the instability of Antarctica's Thwaites Glacier in the 21st century. *Global and Planetary Change*, **153**, 16–34, ISSN 0921-8181 (doi: 10.1016/j.gloplacha.2017.04.008)

Schulson EM and Duval P (2009) *Creep and Fracture of Ice*. Cambridge University Press, Cambridge, ISBN 978-0-521-80620-6 (doi: 10.1017/CBO9780511581397)

Seroussi H, Nakayama Y, Larour E, Menemenlis D, Morlighem M, Rignot E and Khazendar A (2017) Continued retreat of Thwaites Glacier, West Antarctica, controlled by bed topography and ocean circulation. *Geophysical Research Letters*, **44**(12), 6191–6199, ISSN 1944-8007 (doi: 10.1002/2017GL072910)

Seroussi H, Nowicki S, Payne AJ, Goelzer H, Lipscomb WH, Abe-Ouchi A, Agosta C, Albrecht T, Asay-Davis X, Barthel A, Calov R, Cullather R, Dumas C, Galton-Fenzi BK, Gladstone R, Golledge NR, Gregory JM, Greve R, Hattermann T, Hoffman MJ, Humbert A, Huybrechts P, Jourdain NC, Kleiner T, Larour E, Leguy GR, Lowry DP, Little CM, Morlighem M, Pattyn F, Pelle T, Price SF, Quiquet A, Reese R, Schlegel NJ, Shepherd A, Simon E, Smith RS, Straneo F, Sun S, Trusel LD, Van Breedam J, van de Wal RSW, Winkelmann R, Zhao C, Zhang T and Zwinger T (2020) ISMIP6 Antarctica: A multi-model ensemble of the Antarctic ice sheet evolution over the 21st century. *The Cryosphere*, **14**(9), 3033–3070, ISSN 1994-0416 (doi: 10.5194/tc-14-3033-2020)

Shapero DR, Badgeley JA, Hoffman AO and Joughin IR (2021) Icepack: A new glacier flow modeling package in Python, version 1.0. *Geoscientific Model Development*, **14**(7), 4593–4616, ISSN 1991-959X (doi: 10.5194/gmd-14-4593-2021)

Shepherd A, Wingham D, Payne T and Skvarca P (2003) Larsen Ice Shelf Has Progressively Thinned. *Science*, **302**(5646), 856–859 (doi: 10.1126/science.1089768)

Skvarca P (1993) Fast recession of the northern Larsen Ice Shelf monitored by space images. *Annals of Glaciology*, **17**, 317–321, ISSN 0260-3055, 1727-5644 (doi: 10.3189/S0260305500013033)

Stolt RH (1978) Migration by Fourier transform. *Geophysics*, **43**(1), 23–48, ISSN 1942-2156, 0016-8033 (doi: 10.1190/1.1440826)

Tinto KJ and Bell RE (2011) Progressive unpinning of Thwaites Glacier from newly identified offshore ridge: Constraints from aerogravity. *Geophysical Research Letters*, **38**(20), ISSN 1944-8007 (doi: 10.1029/2011GL049026)

Tzanis A (2010) matGPR Release 2: A freeware MATLAB® package for the analysis & interpretation of common and single offset GPR data. *FastTimes*, **15**, 17–43

van den Broeke M (2005) Strong surface melting preceded collapse of Antarctic Peninsula ice shelf. *Geophysical Research Letters*, **32**(12), ISSN 1944-8007 (doi: 10.1029/2005GL023247)

van der Veen CJ (1998a) Fracture mechanics approach to penetration of bottom crevasses on glaciers. *Cold Regions Science and Technology*, **27**(3), 213–223, ISSN 0165-232X (doi: 10.1016/S0165-232X(98)00006-8)

van der Veen CJ (1998b) Fracture mechanics approach to penetration of surface crevasses on glaciers. *Cold Regions Science and Technology*, **27**(1), 31–47, ISSN 0165-232X (doi: 10.1016/S0165-232X(97)00022-0)

Vaughan DG and Doake CSM (1996) Recent atmospheric warming and retreat of ice shelves on the Antarctic Peninsula. *Nature*, **379**(6563), 328–331, ISSN 0028-0836, 1476-4687 (doi: 10.1038/379328a0)

Walker CC, Millstein JD, Miles BWJ, Cook S, Fraser AD, Colliander A, Misra S, Trusel LD, Adusumilli S, Roberts C and Fricker HA (2024) Multi-decadal collapse of East Antarctica's Conger–Glenzer Ice Shelf. *Nature Geoscience*, **17**(12), 1240–1248, ISSN 1752-0908 (doi: 10.1038/s41561-024-01582-3)

Wanzer L (2025) *Terraced Basal Morphology of Thwaites Eastern Ice Shelf, West Antarctica: Insights on Formation and Melt Patterns*. Ph.D. thesis, Oregon State University

Wild CT, Alley KE, Muto A, Truffer M, Scambos TA and Pettit EC (2022) Weakening of the pinning point buttressing Thwaites Glacier, West Antarctica. *The Cryosphere*, **16**(2), 397–417, ISSN 1994-0416 (doi: 10.5194/tc-16-397-2022)

Wild CT, Kachuck SB, Luckman A, Alley KE, Sharp MA, Smith H, Tyler SW, Kratt C, Dotto TS, Price D, Nicholls KW, Bevan SL, Collao-Barrios G, Muto A, Truffer M, Scambos TA, Heywood KJ, Pettit EC and Team tT (2024) Rift propagation signals the last act of the Thwaites Eastern Ice Shelf despite low basal melt rates. *Journal of Glaciology*, **70**, e21, ISSN 0022-1430, 1727-5652 (doi: 10.1017/jog.2024.64)

Wild CT, Alley KE, Luckman A, Greene CA, Gardner AS, Alley R, Truffer M, Sharp MA, Pettit EC, Larter RD and Scambos TA (in prep) Thwaites Glacier ice flux increases during disintegration of its last remaining ice shelf. *Nature Geoscience*

Yu H, Rignot E, Seroussi H and Morlighem M (2018) Retreat of Thwaites Glacier, West Antarctica, over the next 100 years using various ice flow models, ice shelf melt scenarios and basal friction laws. *The Cryosphere*, **12**(12), 3861–3876, ISSN 1994-0416 (doi: 10.5194/tc-12-3861-2018)

# Supplementary Information for *Drivers of The Daggers*: Backstress-triggered fracture propagation on the Thwaites Eastern Ice Shelf, West Antarctica

Meghan A. SHARP[1], Erin C. PETTIT[1]*, Karen E. ALLEY[2], Martin TRUFFER[3], Atsuhiro MUTO[4], Adrian LUCKMAN[5], Christian T. WILD[1,6], Genevieve SAURET[1]

[1]*College of Earth, Ocean, and Atmospheric Science, Oregon State University, Corvallis, OR, USA;* [2]*Centre for Earth Observation Science, Department of Environment and Geography, University of Manitoba, Winnipeg, MB, Canada*

[3]*Geophysical Institute and Dept. Physics, University of Alaska Fairbanks, Fairbanks, Alaska, AK, USA;*

[4]*Department of Earth and Environmental Science, Temple University, Philadelphia, PA, USA;*

[5]*Department of Geography, Faculty of Science and Engineering, Swansea University, UK;*

[6]*Department of Atmospheric and Cryospheric Sciences (ACINN), University of Innsbruck, Innsbruck, Austria*

*Correspondence: Meghan A. Sharp <sharpmeg@oregonstate.edu>*

## CONTENTS

**Supplementary Figures** **1**

Figure S1: Seasonal contribution to annual velocity composites . . . . . 1

Figure S2: Full timeseries of satellite-derived strain rates between 2016-2026 . . . . . 7

## SUPPLEMENTARY FIGURES

### Figure S1: Seasonal contribution to annual velocity composites

*Present address: College of Earth, Ocean, and Atmospheric Sciences, Oregon State University, Corvallis, Oregon, USA.

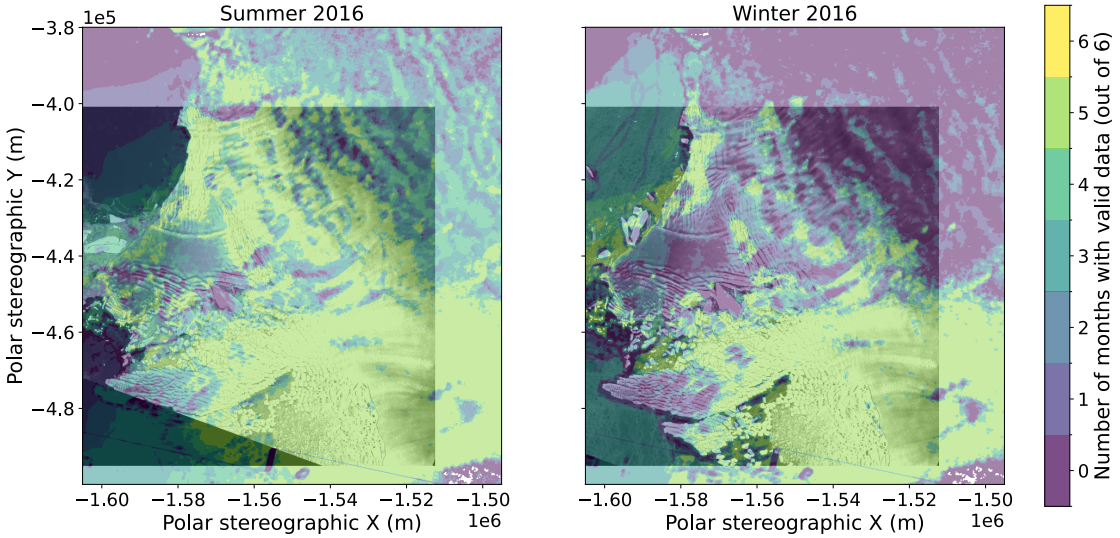



**Fig. S1a.** Number of months in each season contributing to each pixel in the 2016 annual velocity composite. Summer months are: January, February, March, October, November, December (6 total). Winter months are: April, May, June, July, August, September (6 total).

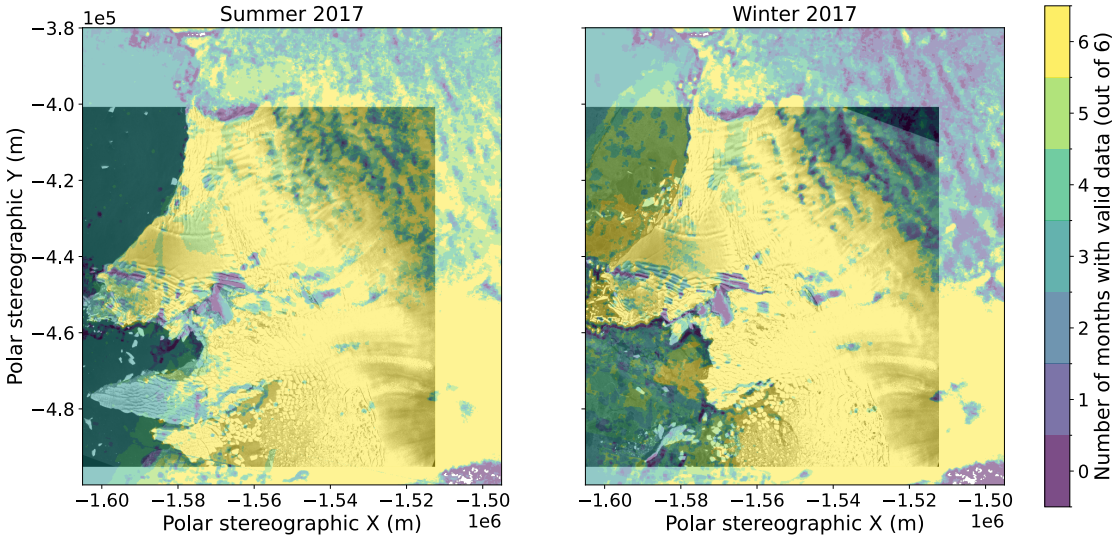



**Fig. S1b.** Same as S1a for 2017.

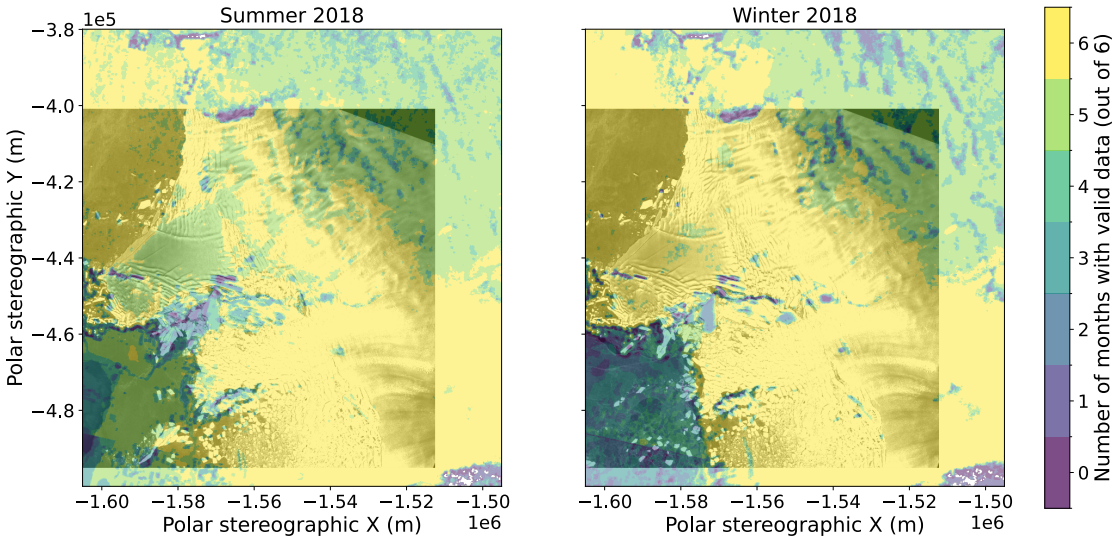



**Fig. S1c.** Same as S1a for 2018.

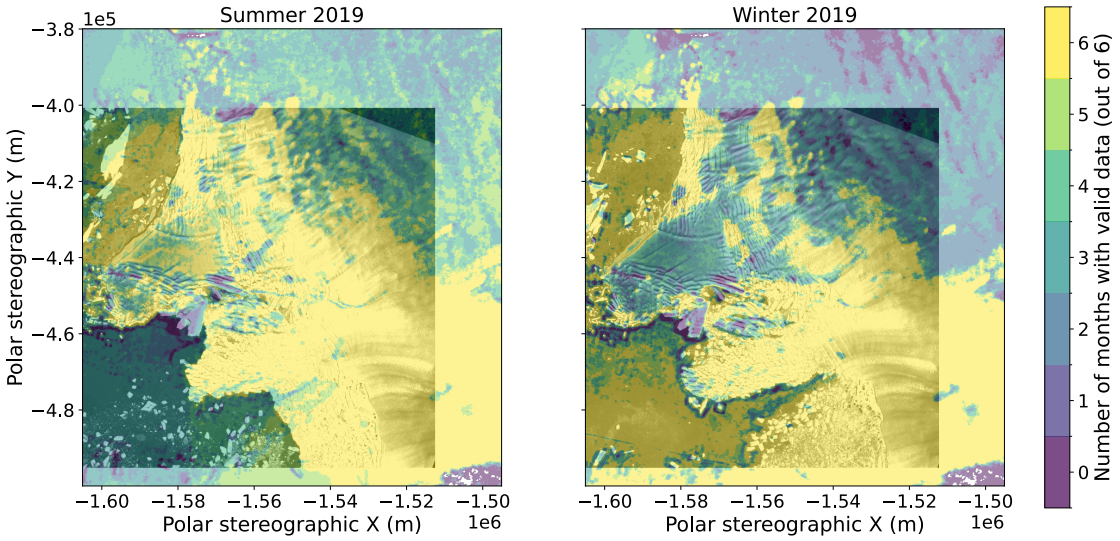



**Fig. S1d.** Same as S1a for 2019.

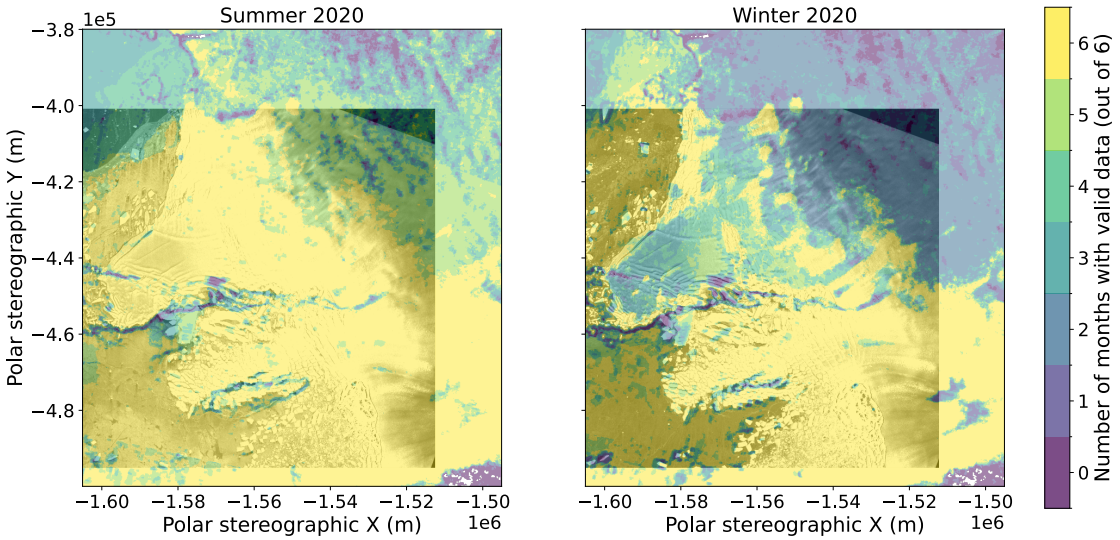



**Fig. S1e.** Same as S1a for 2020.

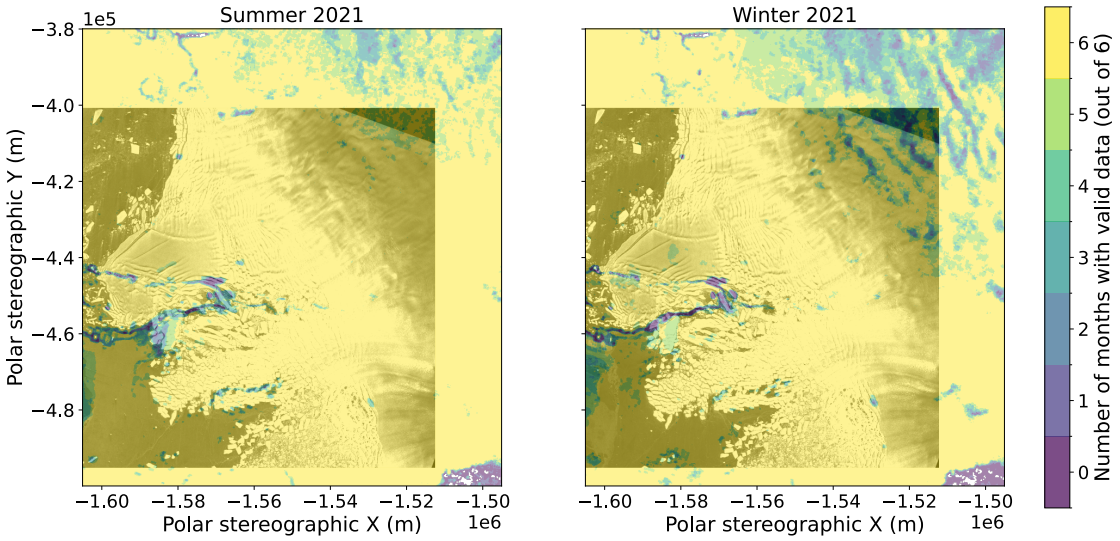



**Fig. S1f.** Same as S1a for 2021.

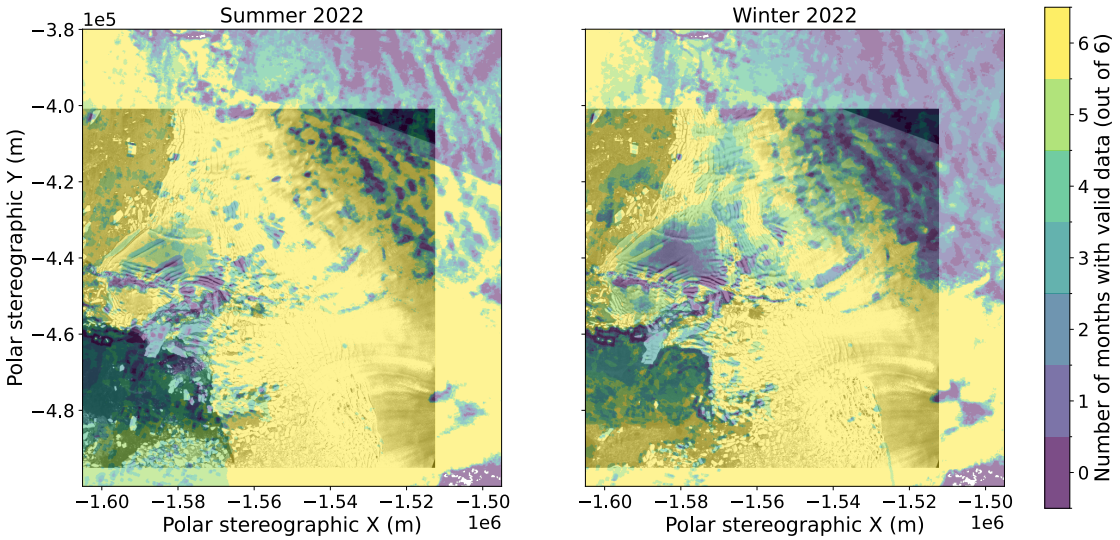



**Fig. S1g.** Same as S1a for 2022.

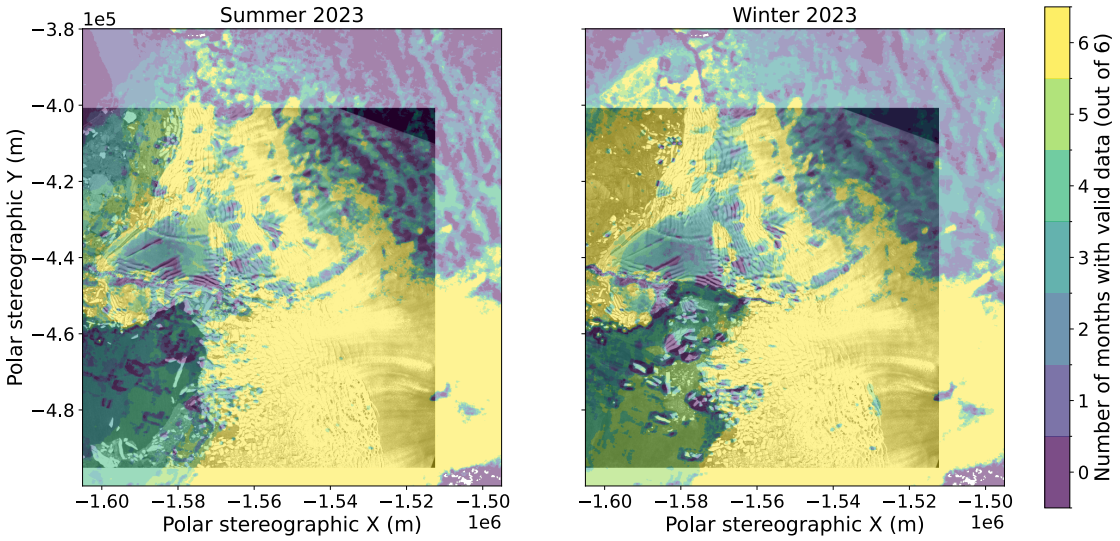



**Fig. S1h.** Same as S1a for 2023.

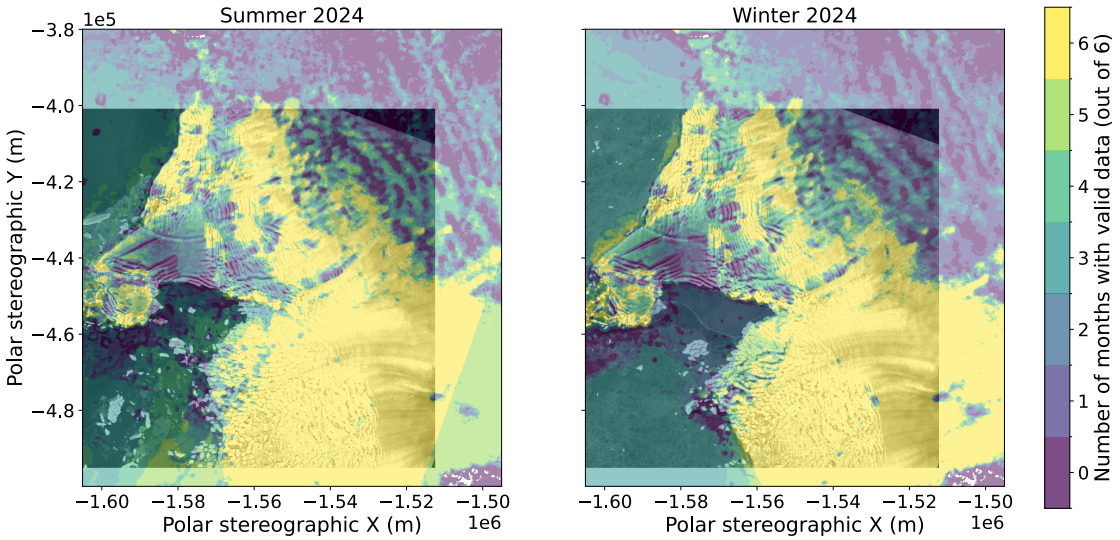



**Fig. S1i.** Same as S1a for 2024.

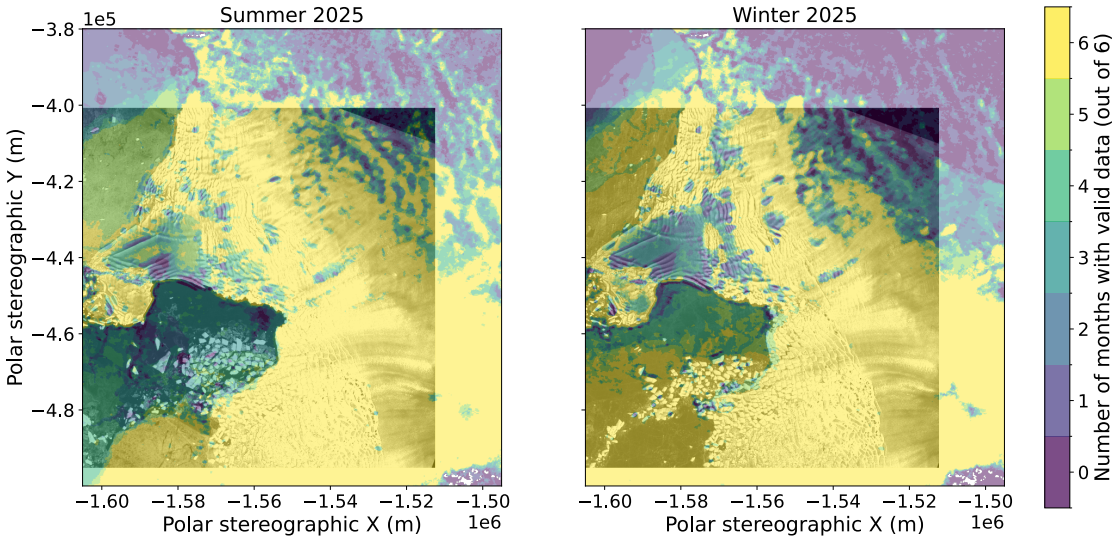



**Fig. S1j.** Same as S1a for 2025.

## Figure S2: Full timeseries of satellite-derived strain rates between 2016-2026

See attached Supplementary_Figure_S2.pdf. Same as Figure 4 in the main text but for all years in the study period.